2007

Improvements to an analytical multiple-shooting approach for optimal burn-coast-burn ascent guidance

Brian Joseph Griffin
Iowa State University

Improvements to an analytical multiple-shooting approach for optimal burn-coast-burn ascent guidance

by

Brian Joseph Griffin

A thesis submitted to the graduate faculty

in partial fulfillment of the requirements for the degree of

MASTER OF SCIENCE

Major: Aerospace Engineering

Program of Study Committee:
Ping Lu, Major Professor
Bion Pierson
Qingze Zou
Frank Chavez

Iowa State University

Ames, Iowa

2007

TABLE OF CONTENTS

LIST OF TABLES

LIST OF FIGURES

ABSTRACT

Launch mission planning and ascent guidance is one of the most notable engineering fields where optimization tools and optimal control theory have found routine applications. Optimality is critical to achieve the full performance of a launch vehicle. In the case of a multi-stage launch, allowing for optimized coast arcs between burns can significantly reduce propellant consumption and enhance mission capability. These coast arcs, however, render the optimal control problem more sensitive and increase algorithm convergence difficulties. This work presents detailed improvements to an analytical multiple-shooting (AMS) method for reliable generation of the optimal exo-atmospheric ascent trajectory. The trajectory consists of two burns separated by an optimized coast arc. The problem is in closed-form and quadratures. A strong effort is made in increasing the robustness, reliability, and flexibility of the algorithm. The improvements include an introduction of a more sophisticated numerical method, replacement of the current coast arc solution with a completely general, compact, and easily implementable method capable of determining the solution to machine precision, and a direct treatment of the orbital insertion conditions and resulting unknown multipliers. An aerospace industry standard trajectory optimization software, Optimal Trajectories by Implicit Simulation (OTIS), is employed to compare the results and verify the improved AMS algorithm. A wide range of mission scenarios are tested using the algorithm in open-loop solution and closed-loop simulation.

CHAPTER 1. INTRODUCTION

1.1 Background

Launch mission planning and ascent guidance is one of the most notable engineering fields where optimization tools and optimal control theory have found routine applications. Optimization is critical to meeting mission requirements such as safety and reliability as well as cost requirements. Goals for NASA's 2^{nd} generation RLV program [1] includes significant improvements in these areas including a requirement to reduce the risk of crew loss to approximately 1 in 10,000 missions while lowering the cost of delivering payloads to low-Earth orbit to less than $1,000 per pound. Indeed, advancements in launch vehicle guidance are not only required, but contribute significantly to achieving such goals [2].

Traditionally, ascent guidance is partitioned into an atmospheric phase and a vacuum phase separated by a predetermined time or event. The atmospheric phase employs an open-loop guidance scheme in which the launch vehicle steering commands are predetermined and obtained via parameter optimization for a given set of vehicle constraints and atmospheric conditions. Any mission or system parameter change requires re-planning of the ascent trajectory and is a labor intensive and time consuming process. However, much research exists aimed at developing robust on-board guidance algorithms for generation of optimal ascent trajectory steering commands in closed-loop for the atmospheric phase of ascent.

The vacuum phase employs a closed-loop guidance scheme in which the launch vehicle steering commands are generated on-board at each guidance cycle and are determined from current conditions including the vehicle state information. When solving the optimal ascent problem on-board repeatedly with the current conditions as the initial conditions, the guidance solution is in effect closed-loop. On-board algorithms for solving the optimal ascent problem

have provided the foundation for upper stage closed-loop ascent guidance dating back to the 1960s. Applications of classical exo-atmospheric optimal ascent guidance algorithms include the Iterative Guidance Mode (IGM) used for the Saturn V rockets [3] and Powered Explicit Guidance (PEG) [4] used on the Space Shuttle. Additionally, an algorithm termed (OPGUID) developed by Brown and Johnson [5] represents another early attempt at closed-loop exo-atmospheric ascent guidance. In this work, the optimal ascent problem is solved as a boundary value problem using a tailored numerical integration algorithm where at each guidance cycle the solution is updated using only a single Newton iteration.

In the case of a multi-stage launch, allowing for an optimized coast arc between two burns is significantly more efficient in propellant consumption and allows for increased deliverable payload mass and increased mission capability. In addition to launch, many orbit transfer problems as well as some mission abort scenarios require the use of multiple burn arcs separated by disproportionately long coast arcs. As a result, much research exists seeking robust and reliable guidance algorithms capable of handling multi-burn trajectory optimization. Some of the earliest research in this area was also done by Brown et. al. [6]. Here an indirect shooting method was developed for optimization of multiple-burn rocket flights. The algorithm, named (SWITCH), was a multi-burn-arc version of the original single-burn-arc algorithm (OPGUID) mentioned previously. Jezewski [7, 8] extended this work by introducing a linear gravity field approximation resulting in reduced computation time with minimal to no loss in solution accuracy. A production algorithm termed 'Gamma Guidance' was developed by Hardtla [10] and was used for the IUS spacecraft. Recent research on multi-burn trajectory optimization addresses atmospheric fight as well. Gath and Calise [11] introduced a hybrid ascent guidance method that was later improved by Calise et. al. [12] to a free final time formulation in which coast arcs are optimized. In another recent effort, Dukeman and Calise [13] develops a numerical multiple-shooting algorithm and introduces alternate forms of the switching conditions which allow for more general terminal conditions. In similar works, Lu et. al. [14] and Zhang [15] present an analytical multiple-shooting (AMS) method within the framework of conventional multiple-shooting, however the propagation of the state/costate is all analytical.

1.2 Overview

The analytical multiple-shooting (AMS) method lays the foundation for the work presented in this thesis and a detailed development of the method is presented. The primary effort in this work is to strive for enhanced robustness and reliability of the algorithm. In addition, efforts are made to further prove the efficiency and validity of the algorithm as a valuable tool in on-board applications for closed-loop ascent guidance. In this approach the optimal trajectory includes segments of burn and coast arcs. Instead of seeking maximum generality, the development in this work is presented in a burn-coast-burn sequence, however as will be discussed, there is no methodological difficulty in extending the development to an arbitrary sequence of burn and coast segments.

Most of the existing work uses the classical or some modified version of the Newton-Raphson method for numerical solutions. One contribution of this thesis is to enhance the reliability and convergence of the algorithm by adopting the highly-regarded Powell's dog-leg method [16]. This method has been proven to converge for problems where the Newton-Raphson method has failed, even for a substantial range of initial guesses.

For the optimized coast arc segment of the ascent trajectory, the current approach opts to solve a Gauss orbit determination problem by implementing the f and g series [25, 26] in orbital mechanics. This method does suffer from some deficiencies wherein the required series coefficients cannot be easily determined recursively from an algorithm implementation viewpoint. Another contribution of this work is to implement Goodyear's method [17, 18] of orbit determination. This method is similar to the f and g series, however Goodyear's method provides a completely general solution for both the state and its partial derivatives. This provides an efficient and easily implementable solution for all cases of two-body motion.

The trajectory terminal conditions introduce unknown Lagrange multipliers that must be addressed in solving the optimal ascent problem. Most of the existing work addresses this by eliminating the unknown multiplier from the problem using either numerical or analytical techniques. This decreases the number of unknowns that must be iterated on when finding the the optimal solution numerically. Adopting Powell's dog-leg method in place of the classical

Newton-Raphson method allows these multipliers to be including as unknowns in the optimal ascent problem with little noticeable decrease in convergence rates. For this reason, this ability has been added to the analytical multiple-shooting algorithm as a user configurable option.

To verify the results obtained from the analytical multiple-shooting method, an industry standard aerospace trajectory optimization software, Optimal Trajectories by Implicit Simulation (OTIS) [19], is used to compute and compare the burn-coast-burn optimal trajectory found under identical conditions. An overview of OTIS and is capabilities will be presented. Furthermore, the analytical multiple-shooting algorithm is used to generate optimal steering commands driving closed-loop simulations under a full nonlinear gravity model. The closed-loop simulations act as checks on the validity of the optimal open-loop trajectories found from the AMS method. If the closed-loop trajectory matches the open-loop one closely, the approximations adopted in the development of the AMS method are justified.

The current algorithm is built on a two-stage launch vehicle framework such that the first burn is of fixed duration determined by the vehicles available propellant. For single-stage launch vehicle missions and orbit transfer missions it is desirable to extend this framework to optimize the first burn as well. Development is presented showing necessary equations enabling this ability.

CHAPTER 2. MATHEMATICAL BACKGROUND

2.1 Optimal Control Theory

Launch vehicle trajectory optimization can have a significant impact on fuel usage for a given payload, or on delieverable payload mass for vehicles of the same gross weight. For these reasons, the need to optimize the guidance commands to meet such objectives becomes very important and some method of optimization is required. Optimal control theory [23, 27] provides the methodology to accomplish this task. Considering the necessity and significance of optimal control theory application to launch vehicle ascent planning and guidance problems, a general overview and brief development of the theory as it applies to the problems of interest is presented below.

2.1.1 Problem Formulation

A general nonlinear time-varying dynamic system can be described by the state equation

$$\dot{\boldsymbol{x}} = \boldsymbol{f}(\boldsymbol{x}, \boldsymbol{u}, t)\,, \quad \boldsymbol{x}(t_0) = \boldsymbol{x}_0 \tag{2.1}$$

where $\boldsymbol{x}(t) \in R^n$ is the system state vector, $\boldsymbol{u}(t) \in R^m$ is the system control input vector, and $\boldsymbol{x}(t_0) = \boldsymbol{x}_0$ is the state at the initial time t_0. A Bolza functional performance index is associated with the system and is of the form

$$J = \phi\left(\boldsymbol{x}_f, t_f\right) + \int_{t_0}^{t_f} L\left(\boldsymbol{x}, \boldsymbol{u}, t\right) dt \tag{2.2}$$

where ϕ and L are scalar functions and in many practical applications the initial time can be set to zero.

The optimal control problem is to find the input $\boldsymbol{u}^*(t), t_0 \leq t \leq t_f$ such that $\boldsymbol{u}^*(t)$ and the corresponding state $\boldsymbol{x}^*(t)$ minimize the performance index in Eq. (2.2) while satisfying the

state equation (2.1) and an additional boundary condition on the final state of the form

$$\boldsymbol{\Psi}\left(\boldsymbol{x}_f, t_f\right) = 0 \tag{2.3}$$

where $\boldsymbol{\Psi} \in R^p$ and $\boldsymbol{x}_f = \boldsymbol{x}(t_f)$ is the state at the final time t_f.

2.1.2 Development

Lagrange multipliers are used to augment the state equation (2.1) and terminal constraints in Eq. (2.3) to the performance index in Eq. (2.2) and is given by

$$J' = \phi\left(\boldsymbol{x}_f, t_f\right) - \boldsymbol{\nu}^T \boldsymbol{\Psi}\left(\boldsymbol{x}_f, t_f\right) + \int_{t_0}^{t_f} \left[L(\boldsymbol{x}, \boldsymbol{u}, t) - \boldsymbol{p}^T\left(\boldsymbol{f}(\boldsymbol{x}, \boldsymbol{u}, t) - \dot{\boldsymbol{x}}\right)\right] dt \tag{2.4}$$

where the constant multiplier $\boldsymbol{\nu} \in R^k$ and the time-varying multiplier $\boldsymbol{p}(t) \in R^n$, referred to as the costate vector, are the Lagrange multipliers augmenting the terminal and dynamic constraints respectively.

A Hamiltonian function is defined as

$$H = \boldsymbol{p}^T \boldsymbol{f}(\boldsymbol{x}, \boldsymbol{u}, t) - L(\boldsymbol{x}, \boldsymbol{u}, t) = \sum_{i=1}^{n} p_i f_i(\boldsymbol{x}, \boldsymbol{u}, t) - L(\boldsymbol{x}, \boldsymbol{u}, t) \tag{2.5}$$

allowing the augmented performance index to be expressed as

$$J' = \phi\left(\boldsymbol{x}_f, t_f\right) - \boldsymbol{\nu}^T \boldsymbol{\Psi}\left(\boldsymbol{x}_f, t_f\right) + \int_{t_0}^{t_f} \left[\boldsymbol{p}^T \dot{\boldsymbol{x}} - H\right] dt \tag{2.6}$$

The constrained minimum of J corresponds to the unconstrained minimum of J' found by determining the increment of J' as a function of increments in $\boldsymbol{x}$, $\boldsymbol{p}$, $\boldsymbol{\nu}$, $\boldsymbol{u}$, and t resulting in the following expression [27].

$$\begin{aligned} dJ' = {} & \left(\phi_x - {\boldsymbol{\Psi}_x}^T \boldsymbol{\nu} + \boldsymbol{p}\right)^T d\boldsymbol{x}\Big|_{t_f} + \left(\phi_t - {\boldsymbol{\Psi}_t}^T \boldsymbol{\nu} - H\right) dt\Big|_{t_f} \\ & - \boldsymbol{\Psi}^T\Big|_{t_f} d\boldsymbol{\nu} - \left(-H + \boldsymbol{p}^T \dot{\boldsymbol{x}} - \boldsymbol{p}^T \dot{\boldsymbol{x}}\right) dt\Big|_{t_0} - \boldsymbol{p}^T d\boldsymbol{x}\Big|_{t_0} \\ & + \int_{t_0}^{t_f} \left[(-H_x - \dot{\boldsymbol{p}}^T)\delta\boldsymbol{x} - H_u \delta\boldsymbol{u} + (-H_p + \dot{\boldsymbol{x}})^T \delta\boldsymbol{p}\right] dt \end{aligned} \tag{2.7}$$

where the x, p, u, and t subscripts refer to partials with respect to that variable.

2.1.3 Necessary Conditions (The Maximum Principle)

The resulting necessary conditions are a set of conditions that $\boldsymbol{u}^*(t)$ and $\boldsymbol{x}^*(t)$ must satisfy. These conditions are given below.

State equation:

$$\dot{\boldsymbol{x}} = \frac{\partial H}{\partial \boldsymbol{p}} = \boldsymbol{f}(\boldsymbol{x}, \boldsymbol{u}, t)\,, \quad t_0 \leq t \leq t_f \tag{2.8}$$

Costate equation:

$$\dot{\boldsymbol{p}} = -\frac{\partial H}{\partial \boldsymbol{x}} = -\frac{\partial f}{\partial \boldsymbol{x}}^T \boldsymbol{p} + \frac{\partial L}{\partial \boldsymbol{x}}, \quad t_0 \leq t \leq t_f \tag{2.9}$$

The optimal solution must satisfy the Pontryagin Maximum Principle of optimality [28] which states that the Hamiltonian must be maximized over all admissible control values $\boldsymbol{u}$ for optimal values of the state and costate. This can be expressed as

$$H(\boldsymbol{x}^*, \boldsymbol{u}^*, \boldsymbol{p}, t) = \max_{\boldsymbol{u}} H(\boldsymbol{x}^*, \boldsymbol{u}, \boldsymbol{p}, t) \tag{2.10}$$

where $*$ represents optimal values. This principle will be useful in determining the optimal control input for the launch vehicle vacuum ascent problem. When the control $\boldsymbol{u}$ is unconstrained the optimality condition (2.10) necessitates the stationarity condition which can be seen from equation (2.7).

Stationarity condition:

$$\frac{\partial H(\boldsymbol{p}, \boldsymbol{x}^*, \boldsymbol{u}^*, t)}{\partial \boldsymbol{u}} = \frac{\partial \boldsymbol{f}}{\partial \boldsymbol{u}}^T \boldsymbol{p} - \frac{\partial L}{\partial \boldsymbol{u}} = 0 \tag{2.11}$$

For the launch vehicle vacuum ascent problem presented later, the final state $\boldsymbol{x}_f$ and the final time t_f are both free and independent allowing the coefficients of $d\boldsymbol{x}|_{t_f}$ and $dt|_{t_f}$ in equation (2.7) to be set to zero independently. This results in two transversality conditions as follows.

Costate Transversality condition:

$$\boldsymbol{p}_f = -\frac{\partial \phi}{\partial \boldsymbol{x}_f} + \frac{\partial \boldsymbol{\Psi}}{\partial \boldsymbol{x}_f}^T \boldsymbol{\nu} \tag{2.12}$$

where $\boldsymbol{p}_f = \boldsymbol{p}(t_f)$ is the costate at the final time t_f.

Hamiltonian Transversality condition:

$$H(t_f) = \frac{\partial \phi}{\partial t_f} - \frac{\partial \boldsymbol{\Psi}}{\partial t_f} \tag{2.13}$$

2.1.4 Additional Conditions

Another important condition derived from the Hamiltonian in Eq. (2.5) is as follows. The time derivative of the Hamiltonian can be expressed as [27]

$$\dot{H} = \frac{\partial H}{\partial t} + \frac{\partial H}{\partial \boldsymbol{x}}^T \dot{\boldsymbol{x}} + \frac{\partial H}{\partial \boldsymbol{u}}^T \dot{\boldsymbol{u}} + \dot{\boldsymbol{p}}^T \boldsymbol{f} = \frac{\partial H}{\partial t} + \frac{\partial H}{\partial \boldsymbol{u}}^T \dot{\boldsymbol{u}} + \left(\frac{\partial H}{\partial \boldsymbol{x}} + \dot{\boldsymbol{p}} \right)^T \boldsymbol{f} \tag{2.14}$$

From the costate equation and stationarity condition above in Eqs. (2.9) and (2.11) respectively, it can be seen that if $\boldsymbol{u}(t)$ is optimal then Eq. (2.14) simplifies to

$$\dot{H} = \frac{\partial H}{\partial t} \tag{2.15}$$

For optimal control problems where the functions $\boldsymbol{f}$ and L are not explicit functions of time, such as the launch vehicle vacuum ascent problem presented later, the above expression simply becomes

$$\dot{H} = 0 \tag{2.16}$$

and the Hamiltonian takes a constant value along the optimal trajectory.

Further, from the Hamiltonian transversality condition in Eq. (2.13), since the functions ϕ and $\boldsymbol{\Psi}$ are not explicit functions of the final time t_f, then

$$H(t_f) = 0 \tag{2.17}$$

and therefore from satisfaction of the condition (2.16), the Hamiltonian is zero over the entire optimal trajectory.

CHAPTER 3. VACUUM ASCENT PROBLEM FORMULATION

3.1 Problem Description

Executing multiple burn sequences separated by optimized coast arcs are theoretically more efficient on fuel usage. In the most general sense, any combination of powered / unpowered stages can be included in the ascent problem, and there are no difficulties extending the methodology presented below to these cases. However, the vacuum ascent problem development presented consists of one optimal coast arc between two powered stages. Using Space Shuttle terminology, the first powered stage is a continuation of endo-atmospheric flight beginning just after the launch vehicle clears the atmosphere and lasts until main engine cut-off (MECO). The optimal coast arc then precedes the second powered stage or orbital maneuver system (OMS) burn. An assumption made for this development is that the initial condition ($\boldsymbol{r}_0$, $\boldsymbol{V}_0$) at the beginning of the first powered stage is known. Also, for the current develpemnt, MECO time is predetermined by the launch vehicle's propellant mass and flow rate. Therefore, the objective of the problem is to optimize the coast arc duration such that the OMS burn will meet orbital insertion conditions while maximizing deliverable payload mass.

3.2 Reference Frames and Transformations

The multi-stage exo-atmospheric ascent guidance problem formulation uses two reference frames:

1. Earth Centered Inertial (ECI)

2. Guidance (Plumbline)

3.2.1 Earth Centered Inertial Frame

In the Earth centered inertial (ECI) frame, the z axis points north along the rotation axis. The x axis lies on the equator along the mean vernal equinox. The y axis completes a right-handed coordinate system. Figure 3.1 illustrates the coordinate system.

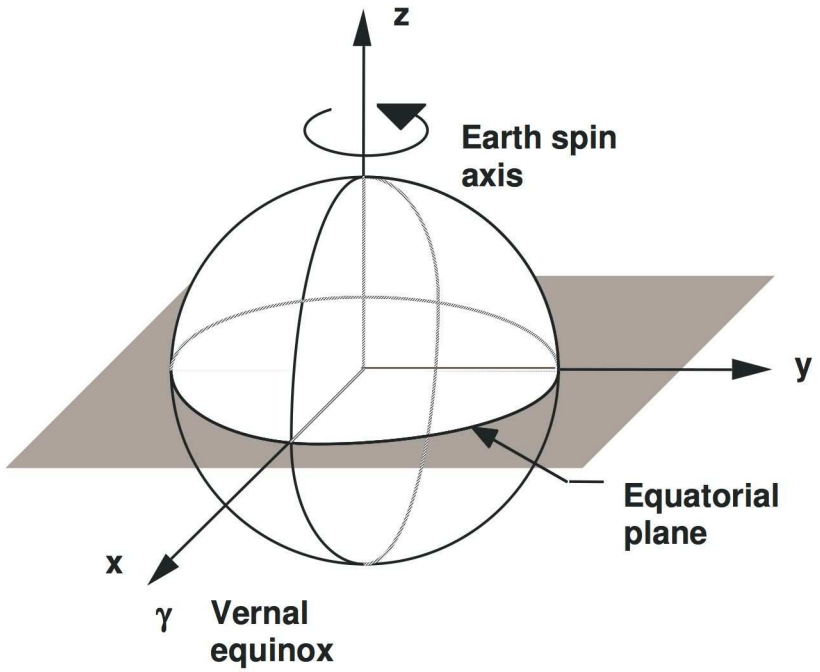

Figure 3.1 Earth Centered Inertial frame

3.2.2 Guidance (Plumbline)

The ascent guidance, or sometimes referred to as plumbline, reference frame is also an Earth centered inertial frame. The x axis points parallel to the launch site local vertical direction and is positive outward. The z axis lies along the launch azimuth or downrange direction. The y axis completes a right-handed coordinate system. The launch azimuth A_z for an ascending orbit is given by:

$$A_z = \sin^{-1}\left(\frac{\cos i}{\cos \Phi_c}\right) \tag{3.1}$$

and for a descending orbit:

$$A_z = \frac{\pi}{2} + \sin^{-1}\left(\frac{\cos i}{\cos \Phi_c}\right) \tag{3.2}$$

where i is the target orbit inclination and Φ_0 the launch site geocentric latitude. Refer to Figure 3.2.

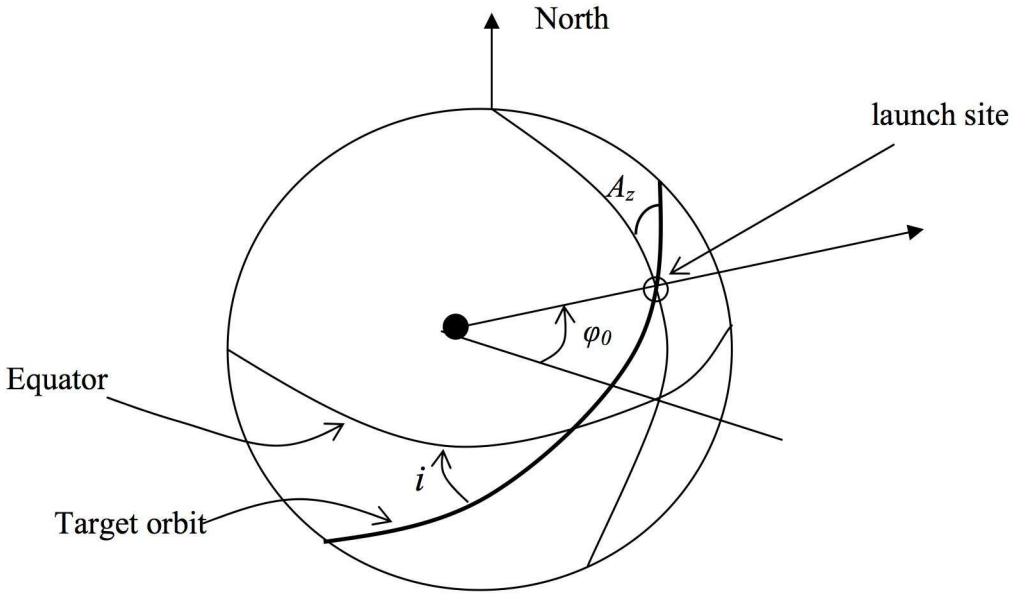

Figure 3.2 Launch site with projected target orbit

3.2.3 Coordinate Transformation

The ascent guidance problem and its solution implementation uses the Guidance inertial reference frame, however it may be useful to convert to the Earth Centered Inertial frame.

Let T_{EG} be the transformation matrix from the ECI to guidance frame. This becomes

$$T_{EG} = \begin{bmatrix} \cos\Theta\cos\Phi_c & \sin\Theta\cos\Phi_c & \sin\Phi_c \\ -\sin\Theta\cos A_z + \cos\Theta\sin\Phi_c\sin A_z & \cos\Theta\cos A_z + \sin\Theta\sin\Phi_c\sin A_z & -\cos\Phi_c\sin A_z \\ -\sin\Theta\sin A_z - \cos\Theta\sin\Phi_c\cos A_z & \cos\Theta\sin A_z - \sin\Theta\sin\Phi_c\cos A_z & \cos\Phi_c\cos A_z \end{bmatrix} \tag{3.3}$$

where Θ and Φ_c are the longitude and geocentric latitude of the launch site respectively. A_z is the launch azimuth defined in Eq. (3.1) and Eq. (3.2).

3.3 Ascent Dynamics

After the launch vehicle reaches an altitude where aerodynamic forces can be ignored the vacuum flight equations of motion become

$$\dot{\boldsymbol{r}} = \boldsymbol{V} \tag{3.4}$$

$$\dot{\boldsymbol{V}} = \boldsymbol{g}(\boldsymbol{r}) + \frac{T\mathbf{1}_T}{m(t)} \tag{3.5}$$

$$\dot{m} = -\frac{T}{g_0 I_{sp}} \tag{3.6}$$

where $\boldsymbol{r} \in R^3$ and $\boldsymbol{V} \in R^3$ are the position and velocity vectors in the guidance inertial frame. Gravitational acceleration is a function of $\boldsymbol{r}$, and g_0 is it's magnitude at some reference radius R_0. The unit vector $\mathbf{1}_T$ defines the direction of the engine thrust with magnitude T. Engine performance defined by the specific impulse I_{sp} is used to determine the vehicles mass flow rate $\dot{m}$. Using another reference radius $\bar{r}$ (e.g., an average value of $\boldsymbol{r}$ along the ascent trajectory), a so-called linear approximation to the gravitational acceleration [9] can be made

$$\boldsymbol{g} = -\frac{\mu}{\bar{r}^2}\frac{\boldsymbol{r}}{\bar{r}} = -\bar{\omega}^2\boldsymbol{r} \tag{3.7}$$

where μ is the Earth's gravitational parameter, and $\bar{\omega} = \sqrt{\mu/\bar{r}^3}$ is the Schuler frequency at $\bar{r}$. This preserves the gravitational acceleration direction in the ascent flight, and enables an analytical solution to the co-state equation in optimal vacuum flight as shown will be shown. Variation in gravitational acceleration magnitude due to this approximation has negligible influence on the solution. One closed-loop guidance algorithm implementation is to at each guidance cycle update $\bar{r}$ thus further minimizing any effects of the approximation.

Convergence of the numerical methods presented in this paper are improved by conditioning problem parameters. Distances are normalized by the reference radius R_0, velocities by $\sqrt{R_0 g_0}$, and time by $\sqrt{R_0/g_0}$. Continuing use of the variables $\boldsymbol{r}$ and $\boldsymbol{V}$, now representing dimensionless parameters, the above equations of motion become

$$\boldsymbol{r}' = \boldsymbol{V} \tag{3.8}$$

$$\boldsymbol{V}' = -\omega^2\boldsymbol{r} + A_T\mathbf{1}_T \tag{3.9}$$

$$m' = -\frac{T}{c} \tag{3.10}$$

where now the differentiation is with respect to the nondimensional time $\tau = t/\sqrt{R_0/g_0}$, $\omega = \sqrt{(R_0/\bar{r})^3}$ is the nondimensional Schuler frequency, $A_T = T/mg_0$ is the instantaneous thrust acceleration in g, and $c = I_{sp}/\sqrt{R_0/g_0^3}$ is piecewise constant that depending on algorithm implementation, can be updated for each powered stage or during each guidance cycle as discussed above.

3.4 Optimal Control Problem

The launch vehicle ascent trajectory optimization objective as mentioned previously is to determine the duration of coast arc to minimize the fuel usage or equivalently maximize payload mass, while meeting orbital insertion conditions.

3.4.1 Performance Index

The thrust direction unit vector $\mathbf{1}_T$ is the control variable to be determined by the optimization problem during the launch vehicle ascent trajectory. The performance index can be written as

$$J = -\int_{\tau_0}^{\tau_f} m' d\tau = \int_{\tau_0}^{\tau_f} \frac{T}{c} d\tau \tag{3.11}$$

where τ_0 is the start of the first powered stage and τ_f is the unknown end time of the OMS burn. Clearly this objective function will maximize the orbital insertion mass $m(\tau_f)$.

3.4.2 Orbital Insertion Conditions

The orbital insertion conditions are specified in terms of k equality constraints ($k \leq 6$) on the final state

$$\Psi(\boldsymbol{r}_f, \boldsymbol{V}_f) = 0 \tag{3.12}$$

From standard optimal control theory, the terminal constraints are adjoined to the performance index in Eq. (3.11) with a constant associated Lagrange multiplier $\boldsymbol{\nu} \in R^k$ which results in

the transversality conditions

$$\boldsymbol{p}_r(\tau_f) = \left(\frac{\partial \Psi}{\partial \boldsymbol{r}_f}\right)^T \boldsymbol{\nu} \tag{3.13}$$

$$\boldsymbol{p}_V(\tau_f) = \left(\frac{\partial \Psi}{\partial \boldsymbol{V}_f}\right)^T \boldsymbol{\nu} \tag{3.14}$$

where $\boldsymbol{p}_r$ and $\boldsymbol{p}_V$ are the costate vectors corresponding to the inertial position and velocity vectors respectively. Typical oribital insertion conditions will include a subset of the six target orbital elements. The 6 transversality conditions in Eqs. (3.13-3.14) can be manipulated into $6-k$ independent conditions by eliminating the Lagrange multipler $\boldsymbol{\nu}$. This decreases the number variables and associated equations required for the guidance algorithm. This manipulation, however, depends on the form of terminal conditions used and may not always be desired, for example when the terminal conditions change during the ascent for unanticipated reasons. The current algorithm implementation [15] uses this manipulation. This work adds the flexibility to solve for the Lagrange multiplier $\boldsymbol{\nu}$ directly.

The final time τ_f of the OMS burn is free and must be determined by the optimal control problem. Also, because the terminal constraints in Eq. (3.12) are independent of the time τ_f, an additional transversality condition must be satisfied and demands that

$$H(\tau_f) = 0 \tag{3.15}$$

This will become useful in regards to the switching functioned described later.

3.4.3 Hamiltonian and Additional Necessary Conditions

Again from standard optimal control theory, the dynamic system in Eqs. (3.8-3.10) are adjoined to the performance index in Eq. (3.11) with a time varying costate vector resulting in the Hamiltonian

$$H = \boldsymbol{p}_r{}^T \boldsymbol{V} - \omega^2 \boldsymbol{p}_V{}^T \boldsymbol{r} + \boldsymbol{p}_V{}^T \mathbf{1}_T A_T - p_m \frac{T}{c} - \frac{T}{c} \tag{3.16}$$

where p_m is the costate variable corresponding to the state variable m. This can be rewritten as

$$H = \boldsymbol{p}_r{}^T \boldsymbol{V} - \omega^2 \boldsymbol{p}_V{}^T \boldsymbol{r} + T\left(\frac{\boldsymbol{p}_V{}^T \mathbf{1}_T}{m g_0} - \frac{p_m}{c} - \frac{1}{c}\right) := H_{NT} + TS \tag{3.17}$$

where H_{NT} is the portion of the Hamiltonian having no thrust influence. A second adjoint dynamical system in the costate must be satisfied.

$$\begin{pmatrix} \boldsymbol{p}_r' \\ \boldsymbol{p}_V' \end{pmatrix} = -\begin{pmatrix} \frac{\partial H}{\partial \boldsymbol{r}} \\ \frac{\partial H}{\partial \boldsymbol{V}} \end{pmatrix} = \begin{pmatrix} \omega^2 \boldsymbol{p}_V \\ -\boldsymbol{p}_r \end{pmatrix} \tag{3.18}$$

Additionally, the optimal control problem must satisfy the optimality condition mentioned previously in section (2.1.3) wherein the thrust direction unit vector $\mathbf{1}_T$ must be chosen to maximize the Hamiltonian (3.17) for optimal values of the state and costate.

$$H(\boldsymbol{x}^*, \boldsymbol{u}^*, \boldsymbol{p}, t) = \max_{\boldsymbol{u}} H(\boldsymbol{x}^*, \boldsymbol{u}, \boldsymbol{p}, t) \tag{3.19}$$

Inspection of Eq. (3.17) requires the control vector $\mathbf{1}_T$ be aligned with the costate vector $\boldsymbol{p}_V$, or $\mathbf{1}_T = \boldsymbol{p}_V / \|\boldsymbol{p}_V\|$. For this reason, the costate vector $\boldsymbol{p}_V$ is also referred to as the primer vector [29].

The second term in Eq. (3.17) involves a switching function S that determines when the vehicle is using full thrust or coasting [14, 13, 30].

$$T = \begin{cases} T_{max} & \text{if } S > 0, \\ 0 & \text{if } S < 0. \end{cases} \tag{3.20}$$

The case when $S = 0$ for finite times is not considered. In the current framework of the burn-coast-burn sequence presented, let τ_{OMS} be the start of the OMS burn. It is then necessary that $S(\tau_{OMS}) = 0$ and $S(\tau) > 0$ for $\tau > \tau_{OMS}$. Noticing that the Hamiltonian is not an explicit function of τ, its value remains constant along an optimal trajectory. Further, it has been seen from Eq. (3.15) that Hamiltonian is zero at τ_f and therefore must be zero along the entire optimal trajectory. This results in an alternative expression

$$H_{NT}(\tau_{OMS}) = 0 \tag{3.21}$$

This equivalent expression avoids the necessity to explicitly compute the costate p_m along the trajectory.

CHAPTER 4. APPROACH

4.1 Analytical Ascent Solutions

The vacuum ascent optimization problem presented above has a semi-analytic solution [30, 15]. The use of the linear gravity approximation in Eq. (3.7) allows a closed-form solution of the costate equation (3.18). This combined with quadratures allows an approximate closed-form solution of the state equations (3.8-3.9). This development is presented below. Again, τ_0 is the start of the first powered stage just after the vehicle exits the atmosphere. Rewrite the costate vectors $\boldsymbol{p}_r$ and $\boldsymbol{p}_V$ in the form

$$\boldsymbol{\lambda}(\tau) = \begin{pmatrix} \boldsymbol{p}_V(\tau) \\ -\boldsymbol{p}_r(\tau)/\omega \end{pmatrix}, \quad \boldsymbol{\lambda}_0 = \begin{pmatrix} \boldsymbol{p}_{V_0} \\ -\boldsymbol{p}_{r_0}/\omega \end{pmatrix} \tag{4.1}$$

where $\boldsymbol{p}_{V_0}$ and $\boldsymbol{p}_{r_0}$ are to be determined initial conditions for the costate at τ_0. It can be verified that for $\tau \geq \tau_0$ the costate equation Eq. (3.18) has closed-form solution

$$\boldsymbol{\lambda}(\tau) = \begin{bmatrix} \cos[\omega(\tau-\tau_0)]I_3 & \sin[\omega(\tau-\tau_0)]I_3 \\ -\sin[\omega(\tau-\tau_0)]I_3 & \cos[\omega(\tau-\tau_0)]I_3 \end{bmatrix} \boldsymbol{\lambda}_0 := \Phi(\tau-\tau_0)\boldsymbol{\lambda}_0 \tag{4.2}$$

where I_3 is a 3×3 unit matrix. Rewrite the state vectors $\boldsymbol{r}$ and $\boldsymbol{V}$ as

$$\boldsymbol{x}(\tau) = \begin{pmatrix} \boldsymbol{r}(\tau) \\ \boldsymbol{V}(\tau)/\omega \end{pmatrix}, \quad \boldsymbol{x}_0 = \begin{pmatrix} \boldsymbol{r}_0 \\ \boldsymbol{V}_0/\omega \end{pmatrix} \tag{4.3}$$

It can be verified that the state equations (3.8-3.9) have the following solution

$$\boldsymbol{x}(\tau) = \begin{bmatrix} \cos[\omega(\tau-\tau_0)]I_3 & \sin[\omega(\tau-\tau_0)]I_3 \\ -\sin[\omega(\tau-\tau_0)]I_3 & \cos[\omega(\tau-\tau_0)]I_3 \end{bmatrix} \boldsymbol{x}_0 + \begin{bmatrix} \int_{\tau_0}^{\tau} \frac{1}{\omega}\sin[\omega(\tau-\sigma)]A_T(\sigma)\mathbf{1}_{PV}(\sigma)\,d\sigma \\ \int_{\tau_0}^{\tau} \frac{1}{\omega}\cos[\omega(\tau-\sigma)]A_T(\sigma)\mathbf{1}_{PV}(\sigma)\,d\sigma \end{bmatrix} \tag{4.4}$$

where $\mathbf{1}_{PV} = \boldsymbol{p}_V/\|\boldsymbol{p}_V\|$ and as already stated is the direction of optimal thrust $\mathbf{1}_T$. Also, note that the thrust acceleration $A_T(\cdot)$ is time varying because the vehicle mass is changing. After some trigonometric manipulation, Eq. (4.4) can be written as

$$\boldsymbol{x}(\tau) = \Phi(\tau - \tau_0)\boldsymbol{x}_0 + \Gamma(\tau)\boldsymbol{I}(\tau, \tau_0) \tag{4.5}$$

where

$$\Gamma(\tau) = \frac{1}{\omega}\begin{bmatrix} \sin(\omega\tau)I_3 & -\cos(\omega\tau)I_3 \\ \cos(\omega\tau)I_3 & \sin(\omega\tau)I_3 \end{bmatrix} \tag{4.6}$$

and

$$\boldsymbol{I}(\tau, \tau_0) = \begin{bmatrix} \boldsymbol{I}_c(\tau, \tau_0) \\ \boldsymbol{I}_s(\tau, \tau_0) \end{bmatrix} \tag{4.7}$$

with

$$\boldsymbol{I}_c(\tau, \tau_0) = \int_{\tau_0}^{\tau} \cos(\omega\sigma)A_T(\sigma)\mathbf{1}_{PV}(\sigma)\, d\sigma := \int_{\tau_0}^{\tau} \boldsymbol{i}_c(\sigma)\, d\sigma \in R^3 \tag{4.8}$$

$$\boldsymbol{I}_s(\tau, \tau_0) = \int_{\tau_0}^{\tau} \sin(\omega\sigma)A_T(\sigma)\mathbf{1}_{PV}(\sigma)\, d\sigma := \int_{\tau_0}^{\tau} \boldsymbol{i}_s(\sigma)\, d\sigma \in R^3 \tag{4.9}$$

The forcing thrust integrals $\boldsymbol{I}_c(\cdot,\cdot)$ and $\boldsymbol{I}_s(\cdot,\cdot)$ can be closely approximated with numerical quadrature formulas. Such formulas include the trapezoidal rule, Simpson's rule, the 3/8-rule, and Milnes rule which are all Newton-Cotes formulas of varying complexity wherein the integrands $\boldsymbol{i}_c$ and $\boldsymbol{i}_s$ are replaced by suitable interpolating polynomials. This approach opts to use Milne's rule [24] with the justification of considerably higher precision with little added computation margin. This leads to the approximations

$$\begin{aligned} \boldsymbol{I}_j(\tau, \tau_0) \;&\approx\; \frac{(\tau - \tau_0)}{90}[7\boldsymbol{i}_j(\tau_0) + 32\boldsymbol{i}_j(\tau_0 + \delta) + 12\boldsymbol{i}_j(\tau_0 + 2\delta) \\ &+\; 32\boldsymbol{i}_j(\tau_0 + 3\delta) + 7\boldsymbol{i}_j(\tau_0 + 4\delta)], \quad j = c, s \end{aligned} \tag{4.10}$$

Note that equation (4.10) requires the values of the primer vector $\boldsymbol{p}_V$ at $\tau_0 + i\delta$ in evaluating the thrust integrals. These values are calculated from the propagation of Eq. (4.2) with the initial guess $\boldsymbol{\lambda}_0$. Also, if $\tau - \tau_0$ grows too large for longer powered stages, additional segments in time grid may be used as necessary to decrease approximation error.

4.2 f and g Series Coast State Propagation

During coast phases where $A_T = 0$, the vehicle position and velocity can still be obtained by propagating Eq. (4.4). This closed-form solution is efficient and convenient in that it does not require any algorithm implementation changes from powered stages. However, the linear gravity approximation allowing this closed-form solution may introduce undesirable error as the coast time increases. In some cases, this error is too dominant to ignore. For this reason, the current approach [15] opts to solve a Guass orbit determination problem implementing the f and g series in orbital mechanics [25, 26]. This gives an alternate method to propagate the state over the coast phase. The inverse-square gravity model is used, and this method does not compromise the solution accuracy even for large coasts having relatively large radial distance changes. In either case, the vehicle state at the end of the coast is uniquely defined by it's state at the beginning and the coast time. The costate $\boldsymbol{\lambda}$ will continue to propagate using Eq. (4.2)

The f and g series is a Taylor series expansion of the state in time, with all coefficients expressed as functions of $\boldsymbol{r}_0$ and $\boldsymbol{V}_0$. Let τ_{MECO} be the instant of Main Engine Cut-Off (MECO) and τ_{OMS} be the start of the second or orbital maneuver system burn. The vehicle state at the end of the coast can be expressed as

$$\boldsymbol{r}_{OMS} = f \cdot \boldsymbol{r}_{MECO} + g \cdot \boldsymbol{V}_{MECO} \tag{4.11}$$

$$\boldsymbol{V}_{OMS} = \dot{f} \cdot \boldsymbol{r}_{MECO} + \dot{g} \cdot \boldsymbol{V}_{MECO} \tag{4.12}$$

where f and g are defined as

$$f(\boldsymbol{r}_0, \boldsymbol{V}_0, \tau) = \sum_{n=0}^{\inf} \frac{(\tau_{OMS} - \tau_{MECO})^n}{n!} F_n \tag{4.13}$$

$$g(\boldsymbol{r}_0, \boldsymbol{V}_0, \tau) = \sum_{n=0}^{\inf} \frac{(\tau_{OMS} - \tau_{MECO})^n}{n!} G_n \tag{4.14}$$

where F_n and G_n are the series coefficients and can be found in Reference 25. The derivatives $\dot{f}$ and $\dot{g}$ are with respect to coast duration.

4.3 Multiple Shooting Formulation

The solution to the optimal vacuum ascent problem is, in principle, reduced to a root-finding problem.The problem consists of 8 unknowns: $\boldsymbol{p}_{r_0} \in R^3$, $\boldsymbol{p}_{V_0} \in R^3$, τ_{OMS}, and τ_f. Directly solving for the unknowns is in essence a single-shooting approach.

The single-shooting approach can suffer from sensitivity problems in the burn-coast-burn sequence presented. This is amplified by increasingly long coast times and low thrust magnitude OMS burns. Regarding rapid mission planning, and especially the ability for in flight mission changes, the robustness of the algorithm is of the highest importance. To this end, algorithm convergence is enhanced using a multiple-shooting formulation [24] adding two additional nodes to the numerical problem [13, 15, 30]. One node is placed at the end of first burn, τ_{MECO}. Recall that this time is considered specified by propellant availability. The second node is placed at τ_{OMS}, where the coast ends and the second burn begins. The formulation is illustrated in Figure 4.1. A solution vector stacked with the state and costate is defined and expressed in compact form as

$$\boldsymbol{y}(\tau) = \begin{pmatrix} \boldsymbol{x}(\tau) \\ \boldsymbol{\lambda}(\tau) \end{pmatrix} \in R^{12} \tag{4.15}$$

The propagation of $\boldsymbol{y}$ along the first burn interval (τ, τ_{MECO}) is determined by the initial condition $\boldsymbol{y}_0$ at τ_0 and the closed form solutions given by Eqs. (4.2) and (4.5). The propagated value of $\boldsymbol{y}$ at τ_{MECO} is denoted by $\boldsymbol{y}^-_{MECO}$ indicating its value as $\tau \to \tau_{MECO}$ from the left. At both nodes added to the formulation, introduce a to-be-determined vector

$$\boldsymbol{y}^+_{MECO} = \begin{pmatrix} \boldsymbol{x}^+_{MECO} \\ \boldsymbol{\lambda}^+_{MECO} \end{pmatrix} \tag{4.16}$$

$$\boldsymbol{y}^+_{OMS} = \begin{pmatrix} \boldsymbol{x}^+_{OMS} \\ \boldsymbol{\lambda}^+_{OMS} \end{pmatrix} \tag{4.17}$$

where the + denotes guessed solution vectors at their respective nodes. The propagation of $\boldsymbol{y}$ along the coast arc in the interval (τ_{MECO}, τ_{OMS}) is now determined from from the guessed solution vector $\boldsymbol{y}^+_{MECO}$ as the starting condition. The costate is again computed from the

closed-from solution in Eq. (4.2), however the vehicle state during the coast is computed using the f and g series in Eqs. (4.11) and (4.12). Again, the propagated value of $\boldsymbol{y}$ at τ_{OMS} is denoted by $\boldsymbol{y}^{-}_{OMS}$ indicating its value as $\tau \rightarrow \tau_{OMS}$ from the left. Finally, the propagation of $\boldsymbol{y}$ during the second burn interval (τ_{OMS}, τ_f) is computed similarly to the first burn but with $\boldsymbol{y}^{+}_{OMS}$ as the starting condition. The addition of the nodes to the formulation and their to-be-determined vectors $\boldsymbol{y}^{+}_{MECO}$ and $\boldsymbol{y}^{+}_{OMS}$ requires the following continuity conditions

$$\boldsymbol{y}^{-}_{MECO} - \boldsymbol{y}^{+}_{MECO} = 0 \tag{4.18}$$

$$\boldsymbol{y}^{-}_{OMS} - \boldsymbol{y}^{+}_{OMS} = 0 \tag{4.19}$$

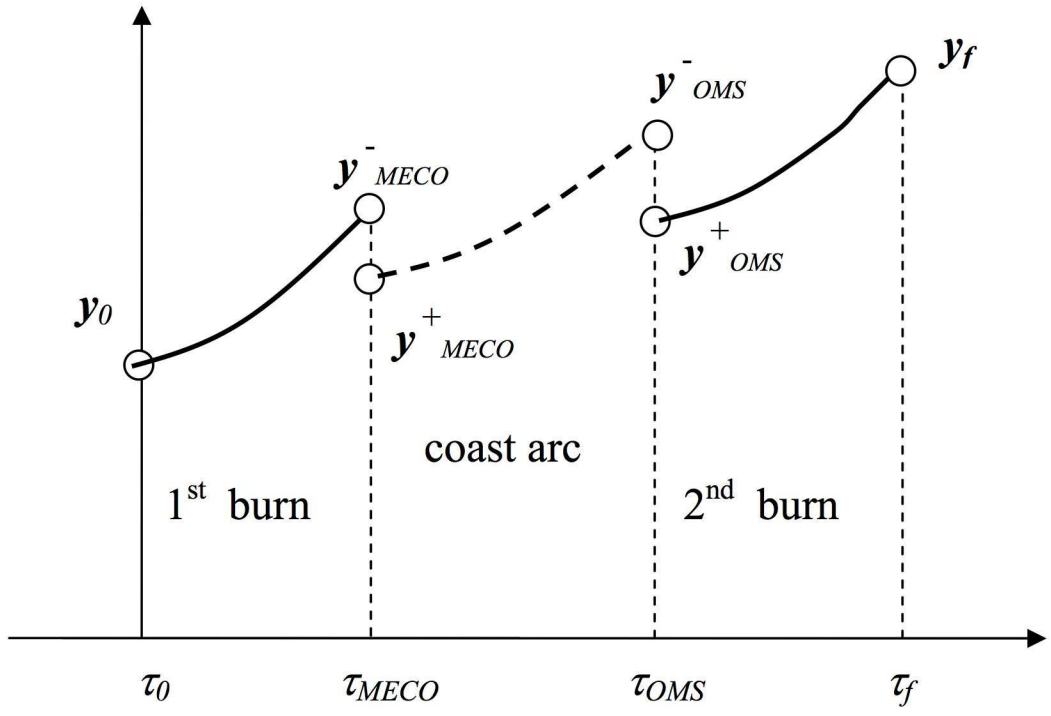

Figure 4.1 Multiple-shooting formulation

This multiple-shooting formulation increases the total number of unknowns by 24 with the introduction of $\boldsymbol{y}^{+}_{MECO} \in R^{12}$ and $\boldsymbol{y}^{+}_{OMS} \in R^{12}$. The continuity conditions in Eqs. (4.18) and (4.19) provide exactly the same number of equations and thus the dimension of the root finding problem is increased to $8 + 24 = 32$. The introduction of the linear gravity approximation and

thrust quadratures make the problem completely analytical, both in function evaluation and its Jacobian computation. The unknowns and constraints of the problem are summarized below.

4.4 Equality Constraints

As discussed previously, a current algorithm implementation [15] eliminates the terminal constraint Lagrange multiplier $\boldsymbol{\nu}$ from the problem formulation. The unknowns in the problem are given as

$$\boldsymbol{z} = (\boldsymbol{\lambda}_0,\, \boldsymbol{\lambda}^+_{MECO},\, \boldsymbol{x}^+_{MECO},\, \tau_{OMS},\, \boldsymbol{\lambda}^+_{OMS},\, \boldsymbol{x}^+_{OMS},\, \tau_f) \in R^{32} \tag{4.20}$$

The vacuum ascent solution is found from 32 equality constraints that $\boldsymbol{z}$ must meet. These constraints include those required from the optimization problem in section (3.4) and the continuity conditions introduced in section (4.3). The continuity conditions in Eqs. (4.18) and (4.19) take the form

$$\boldsymbol{s}_1(\boldsymbol{z}) = \Phi(\tau_{MECO} - \tau_0)\boldsymbol{\lambda}_0 - \boldsymbol{\lambda}^+_{MECO} = 0 \tag{4.21}$$

$$\boldsymbol{s}_2(\boldsymbol{z}) = \Phi(\tau_{MECO} - \tau_0)\boldsymbol{x}_0 + \Gamma(\tau_{MECO})\boldsymbol{I}^0(\tau_{MECO}, \tau_0) - \boldsymbol{x}^+_{MECO} = 0 \tag{4.22}$$

$$\boldsymbol{s}_3(\boldsymbol{z}) = \Phi(\tau_{OMS} - \tau_{MECO})\boldsymbol{\lambda}^+_{MECO} - \boldsymbol{\lambda}^+_{OMS} = 0 \tag{4.23}$$

$$\boldsymbol{s}_4(\boldsymbol{z}) = \boldsymbol{x}_{fg}(\tau_{OMS} - \tau_{MECO}, \boldsymbol{x}^+_{MECO}) - \boldsymbol{x}^+_{OMS} = 0 \tag{4.24}$$

where the thrust integral $\boldsymbol{I}^0(\tau_{MECO}, \tau_0) = (\boldsymbol{I}^0_c, \boldsymbol{I}^0_s)^T$ has components defined in Eqs. (4.8-4.9) and $\boldsymbol{\lambda}$, propagated by Eq. (4.2) with $\boldsymbol{\lambda}_0$, is used in computation of the primer vector direction $\mathbf{1}_{PV}(\cdot)$. The vehicle state vector $\boldsymbol{x}$ at τ_{OMS} is computed with the f and g series with initial condition $\boldsymbol{x}^+_{MECO}$ and is represented above as $\boldsymbol{x}_{fg}(\tau_{OMS} - \tau_{MECO}, \boldsymbol{x}^+_{MECO})$. The above conditions in Eqs. (4.21-4.22) provide 24 constraint equations. The switching condition in Eq. (3.21) between the end of the coast arc and start of the second burn at τ_{OMS} is expressed as

$$s_5(\boldsymbol{z}) = {\boldsymbol{\lambda}^+_{OMS}}^T \boldsymbol{x}^+_{OMS} = 0 \tag{4.25}$$

This provides one additional constraint equation. The final vehicle state and costate, determined in the interval $(\tau_{OMS},\, \tau_f)$ by propagating Eqs. (4.2) and (4.5) with initial conditions

$\boldsymbol{\lambda}^+_{OMS}$ and $\boldsymbol{x}^+_{OMS}$, are expressed as

$$\boldsymbol{\lambda}_f = \Phi(\tau_f - \tau_{OMS})\boldsymbol{\lambda}^+_{OMS} \tag{4.26}$$

$$\boldsymbol{x}_f = \Phi(\tau_f - \tau_{OMS})\boldsymbol{x}^+_{OMS} + \Gamma(\tau_f)\boldsymbol{I}^{OMS+}(\tau_f, \tau_{OMS}) \tag{4.27}$$

where again the thrust integral $\boldsymbol{I}^{OMS+}(\tau_f, \tau_{OMS}) = (\boldsymbol{I}^{OMS+}_c, \boldsymbol{I}^{OMS+}_s)^T$ has components defined in Eqs. (4.8-4.9) and $\boldsymbol{\lambda}$, propagated by Eq. (4.2) with $\boldsymbol{\lambda}^+_{OMS}$, is used in computation of the primer vector direction $\mathbf{1}_{PV}(\cdot)$. As mentioned previously in section (3.4.2), the trasversality conditions are manipulated into $6-k$ independent conditions that, when combined with the k orbital insertion conditions in Eq. (3.12), constitute another 6 constraint equations in the form

$$\boldsymbol{s}_6(\boldsymbol{z}) = \boldsymbol{s}_6(\boldsymbol{x}_f, \boldsymbol{\lambda}_f) = 0 \tag{4.28}$$

The specific form of Eq. (4.28) will depend on the set or orbital insertion conditions. The final equality constraint is the transversality condition on the Hamiltonian $H(\tau_f) = 0$ (see Eq. 3.15). This constraint can be simplified and even under certain conditions eliminated and replaced by a trivial constraint [30]. This last constraint can be expressed as

$$s_7(\boldsymbol{z}) = H(\tau_f) = 0 \tag{4.29}$$

The optimal ascent problem is reduced to a multivariate zero-finding problem of a system of 32 nonlinear algebraic equations

$$\boldsymbol{s}(\boldsymbol{z}) = 0, \quad \boldsymbol{z} \in R^{32} \tag{4.30}$$

where $\boldsymbol{s}(\cdot) = (\boldsymbol{s}_1, \boldsymbol{s}_2, \boldsymbol{s}_3, \boldsymbol{s}_4, s_5, \boldsymbol{s}_6, s_7) : R^{32} \rightarrow R^{32}$ is a smooth vector function.

4.5 Modified Newton-Raphson Method

The classical Newton-Raphson method is simple, efficient, and possibly the most commonly used numerical algorithm for solving nonlinear algebraic equations. The current approach adopts this method and introduces a small modification aimed at enhancing algorithm convergence. A set of general nonlinear algebraic equations can be expressed in the form below.

$$f_i(\boldsymbol{x}) = f_i(x_1, x_2, ..., x_n) = 0, \quad i = 1, 2, \ldots, n \tag{4.31}$$

At each iteration, the current solution estimate $\boldsymbol{x}^{(k)}$ is replaced by a new estimate

$$\boldsymbol{x}^{(k+1)} = \boldsymbol{x}^{(k)} + \boldsymbol{\delta}^{(k)} \tag{4.32}$$

where $\boldsymbol{\delta}^{(k)}$ solves the linear system

$$\boldsymbol{f}(\boldsymbol{x}^{(k)}) = \boldsymbol{f}'(\boldsymbol{x}^{(k)})\boldsymbol{\delta}^{(k)} \tag{4.33}$$

where

$$\boldsymbol{f}'(\boldsymbol{x}^{(k)}) = \left[\frac{d\boldsymbol{f}}{d\boldsymbol{x}}\right]_{\boldsymbol{x}=\boldsymbol{x}^{(k)}} \tag{4.34}$$

is the Jacobian of the system in Eq. (4.31). Given a good initial estimate, this method usually converges quickly to a solution, however, under certain circumstances it is susceptible to various weaknesses causing the method to diverge rapidly or even converge to an undesired or incorrect solution. Two such weaknesses arise when the initial estimate is far from the solution and when the Jacobian matrix is or nearly is singular.

A strategy used to increase convergence reliability is to restrict the predicted step size, but retain its direction. The current solution $\boldsymbol{x}^{(k)}$ is now replaced by the new estimate

$$\boldsymbol{x}^{(k+1)} = \boldsymbol{x}^{(k)} + \gamma^{(k)}\boldsymbol{\delta}^{(k)} \tag{4.35}$$

where $\gamma^{(k)}$ is determined to prevent the new estimate $\boldsymbol{x}^{(k+1)}$ from being worse than the original estimate $\boldsymbol{x}^{(k)}$. Let the sum of squares of residuals be expressed as

$$F(\boldsymbol{x}) = \boldsymbol{f}^T(\boldsymbol{x})\boldsymbol{f}(\boldsymbol{x}) \tag{4.36}$$

The step size parameter $\gamma^{(k)}$ is calculated to achieve the improvement

$$F(\boldsymbol{x}^{(k+1)}) < F(\boldsymbol{x}^{(k)}) \tag{4.37}$$

The current algorithm implementation determines $\gamma^{(k)}$ from

$$\gamma^{(k)} = \max_j \left\{ \frac{1}{2^j} \,\middle|\, F(\boldsymbol{x}^{(k)} + \frac{1}{2^j}\boldsymbol{\delta}^{(k)}) < F(\boldsymbol{x}^{(k)}) \right\}, \quad j = 0, 1, 2, \ldots \tag{4.38}$$

wherein $\gamma^{(k)}$ is halved until Eq. (4.38) is satisfied. This is applied to the system of equations outlined in section (4.4). A solution $\boldsymbol{z}$ is sought satisfying Eq. (4.30) where the required system Jacobian $\frac{d\boldsymbol{s}(\boldsymbol{z})}{d\boldsymbol{z}} \in R^{32\times 32}$ is determined analytically using the state and costate solutions above in section (4.1).

CHAPTER 5. POWELL'S HYBRID DOGLEG METHOD

5.1 Introduction

The modified Newton-Raphson method above provides more reliable convergence than the classical method when the initial estimate is far from the solution; however it still has its deficiencies. It has been proven [16] that for certain systems this method will converge to an incorrect solution even for a substantial range of initial estimates.

5.2 Levenberg-Marquardt Method

Yet another modification to the classical Newton-Raphson method which overcomes this deficiency is the Levenberg-Marquardt method [16]. Here the current solution $\boldsymbol{x}^{(k)}$ is replaced with the new estimate

$$\boldsymbol{x}^{(k+1)} = \boldsymbol{x}^{(k)} + \boldsymbol{\eta}^{(k)} \tag{5.1}$$

such that $\boldsymbol{\eta}^{(k)}$ solves a linear system of the form

$$\left\{\mu^{(k)} I_n + \boldsymbol{f}'(\boldsymbol{x}^{(k)})^T \boldsymbol{f}'(\boldsymbol{x}^{(k)})\right\} \boldsymbol{\eta}^{(k)} = -\boldsymbol{f}'(\boldsymbol{x}^{(k)})^T \boldsymbol{f}(\boldsymbol{x}^{(k)}) \tag{5.2}$$

where I_n is a n dimensional unit matrix and $\mu^{(k)}$, similar to $\gamma^{(k)}$ in Eq. (4.35), is a positive number whose value is calculated to provide the improvement given by Eq. (4.37). When the parameter $\mu^{(k)} = 0$, Eq. (5.2) becomes just the classical Newton-Raphson iteration, and if $\mu^{(k)}$ is large the solution will tend to a small negative multiple of the gradient of $F(\boldsymbol{x})$ at $\boldsymbol{x} = \boldsymbol{x}^{(k)}$ given as

$$\boldsymbol{\eta}^{(k)} \approx -\boldsymbol{f}'(\boldsymbol{x}^{(k)})\boldsymbol{f}(\boldsymbol{x}^{(k)}))/\mu^{(k)} = -\frac{1}{2}\left[\frac{d}{d\boldsymbol{x}} F(\boldsymbol{x})\right]_{\boldsymbol{x}=\boldsymbol{x}^{(k)}} /\mu^{(k)} \tag{5.3}$$

Therefore this iteration blends the classical method with the steepest descent method applied to the function $F(\boldsymbol{x})$.

5.3 Hybrid Dogleg Development

Powell's Hybrid Dogleg method is very similar to the Levenberg-Marquardt method and provides improved reliability over the modified Newton-Raphson method. This more sophisticated method is adopted to replace the modified Newton-Raphson in the current implementation. Aside from this methods enhanced performance, two additional attractive and notable differences from its competitors include

(i) Explicit expressions for the Jacobian matrix $\boldsymbol{f}'(\boldsymbol{x})$ are not required.

(ii) One of two stopping conditions will be satisfied in a finite number of iterations.

The algorithm description, in the case where explicit expressions for the Jacobian are available, outlined in [16], is presented below. Again, it should be noted that an analytical Jacobian is preferable, but not required.

An iteration of the hybrid dogleg method requires the current solution estimate $\boldsymbol{x}^{(k)}$, a step length $\Delta^{(k)}$, and two parameters E and M. The step length $\Delta^{(k)}$, again similar to $\gamma^{(k)}$ in Eq. (4.35) and $\mu^{(k)}$ in Eq. (5.2), is calculated to restrict the displacement from $\boldsymbol{x}^{(k)}$ ensuring a decrease in the value of $F(\boldsymbol{x})$. However, it is desired to keep $\Delta^{(k)}$ as large as possible to prevent the algorithm from performing an unnecessarily high number of iterations to convergence. The parameters E and M are positive fixed parameters that govern the stopping conditions of the algorithm. The iteration stops if the function $F(\boldsymbol{x})$ becomes less than E, or if the distance from $\boldsymbol{x}^{(k)}$ to the predicted solution $\boldsymbol{x}^{(k+1)}$ exceeds M due to a small gradient of $F(\boldsymbol{x})$. Therefore, M is set to an over-estimate of the distance from $\boldsymbol{x}^1$ to the problem solution to ensure its related stopping condition is only met if the algorithm is converging to a stationary point of $F(\boldsymbol{x})$, and E is set to some very small error tolerance value.

The algorithm first calculates both the full classical Newton-Raphson correction $\boldsymbol{\delta}^{(k)}$ and the gradient of $F(\boldsymbol{x})$ at $\boldsymbol{x}^{(k)}$ given by

$$\boldsymbol{g}^{(k)} = 2\boldsymbol{f}'(\boldsymbol{x}^{(k)})\boldsymbol{f}(\boldsymbol{x}^{(k)}) \tag{5.4}$$

A stopping condition test of the form

$$F(\boldsymbol{x}^{(k)}) \geq M\|\boldsymbol{g}^{(k)}\|_2 \tag{5.5}$$

is performed and if it holds the iteration is finished due to the likelihood that $\boldsymbol{x}^{(k)}$ is converging to a local minimum of $F(\boldsymbol{x})$. Note this test is not influenced by singularity in the Jacobian.

If the test in Eq. (5.5) does not hold then a new displacement $\bar{\boldsymbol{\delta}}^{(k)}$ is calculated. This displacement is just set to the classical Newton-Raphson displacement if the condition $\Delta^{(k)} \geq \|\boldsymbol{\delta}^{(k)}\|$ holds; otherwise the displacement takes the form

$$\bar{\boldsymbol{\delta}}^{(k)} = \alpha_1 \boldsymbol{\delta}^{(k)} - \beta_1 \boldsymbol{g}^{(k)} \tag{5.6}$$

where α_1 and β_1 are positive scalars such that

$$\|\bar{\boldsymbol{\delta}}^{(k)}\|_2 = \Delta^{(k)} \tag{5.7}$$

A first attempt is to step along the steepest descent direction of $F(\boldsymbol{x})$ whereby $\alpha_1 = 0$ and

$$\bar{\boldsymbol{\delta}}^{(k)} = -\beta_1 \boldsymbol{g}^{(k)}, \quad \beta_1 = \Delta^{(k)}/\|\boldsymbol{g}^{(k)}\|_2 \tag{5.8}$$

under the condition that this step does not go beyond the predicted minimum point of $F(\boldsymbol{x})$ along this direction given by

$$\boldsymbol{x}^{(k)} - \left\{ \tfrac{1}{2}\|\boldsymbol{g}^{(k)}\|_2^2 / \|\boldsymbol{f}'(\boldsymbol{x}^{(k)})\boldsymbol{g}^{(k)}\|_2^2 \right\} \boldsymbol{g}^{(k)} \tag{5.9}$$

To ensure this condition, another test on $\Delta^{(k)}$ of the from

$$\Delta^{(k)} \leq \tfrac{1}{2}\|\boldsymbol{g}^{(k)}\|_2^3 / \|\boldsymbol{f}'(\boldsymbol{x}^{(k)})\boldsymbol{g}^{(k)}\|_2^2 \tag{5.10}$$

must be satisfied. If the condition in Eq. (5.10) is violated, the new solution estimate $\{\boldsymbol{x}^{(k)} + \bar{\boldsymbol{\delta}}^{(k)}\}$ lies on a line connecting the point given by the Newton-Raphson method $\{\boldsymbol{x}^{(k)} + \boldsymbol{\delta}^{(k)}\}$ to the point given in Eq. (5.9) such that unique values for α_1 and β_1 are determined by satisfying the length condition in Eq. (5.7). The displacement $\bar{\boldsymbol{\delta}}^{(k)}$ is now specified for all cases and it can be seen that the algorithm interpolates between the classical Newton-Raphson method and the steepest descent method.

The function value $\boldsymbol{f}(\boldsymbol{x}^{(k)} + \bar{\boldsymbol{\delta}}^{(k)})$ is evaluated and if the expected equality

$$F(\boldsymbol{x}^{(k)} + \bar{\boldsymbol{\delta}}^{(k)}) < F(\boldsymbol{x}^{(k)}) \tag{5.11}$$

holds, then algorithm defines the new solution estimate $\boldsymbol{x}^{(k+1)} = \boldsymbol{x}^{(k)} + \bar{\boldsymbol{\delta}}^{(k)}$ and a second stopping convergence test of the form

$$F(\boldsymbol{x}^{(k+1)}) < E \tag{5.12}$$

is performed. However, if the condition in Eq. (5.11) does not hold then the algorithm defines $\boldsymbol{x}^{(k+1)} = \boldsymbol{x}^{(k)}$ and the step length $\Delta^{(k)}$ must be reduced for the next iteration.

Revising the step length $\Delta^{(k)}$ depends on the predicted value of the sum of squares of residuals at $\boldsymbol{x}^{(k)} + \bar{\boldsymbol{\delta}}^{(k)}$ given by

$$\Upsilon^{(k)} = \left\{ \boldsymbol{f}(\boldsymbol{x}^{(k)}) + \boldsymbol{f}'(\boldsymbol{x}^{(k)}) \bar{\boldsymbol{\delta}}^{(k)} \right\}^2 \tag{5.13}$$

This value, which is less than $F(\boldsymbol{x}^{(k)})$, is used in a test given by

$$F(\boldsymbol{x}^{(k)} + \bar{\boldsymbol{\delta}}^{(k)}) > (1 - \epsilon) F(\boldsymbol{x}^{(k)}) + \epsilon \Upsilon^{(k)} \tag{5.14}$$

where ϵ, $0 < \epsilon < 1$, is a defined constant. If this passes, it is assumed that the Jacobian $\boldsymbol{f}'(\boldsymbol{x}^{(k)})$ does not adequately approximate $\boldsymbol{f}(\boldsymbol{x})$ over the distance $\|\bar{\boldsymbol{\delta}}^{(k)}\|_2$ and therefore $\Delta^{(k)}$ is reduced by a constant factor ζ, $0 < \zeta < 1$. As mentioned previously, it is desired to keep $\Delta^{(k)}$ as large as possible to decrease the total number of iterations, thus if the condition in Eq. (5.14) fails, $\Delta^{(k)}$ may be increased by some strategy such that the condition $\Delta^{(k+1)} \leq D\Delta^{(k)}$, $D > 1$ for a constant D is satisfied.

This is applied to the system of equations outlined in section (4.4). A solution $\boldsymbol{z}$ is sought satisfying Eq. (4.30) where the required system Jacobian $\frac{d\boldsymbol{s}(\boldsymbol{z})}{d\boldsymbol{z}} \in R^{32\times 32}$ is determined analytically using the state and costate solutions above in section (4.1).

CHAPTER 6. GOODYEAR TWO-BODY PROBLEM

6.1 Introduction

As presented in section (4.2), the current approach opts to solve a Gauss orbit determination problem implementing the f and g series in orbital mechanics. This approach provides a more accurate solution than simply continuing the propagation of the launch vehicle's state using the closed form solution (4.4) as a result of the linear gravity approximation, however, the the required series coefficients in equations (4.13-4.14) and their partial derivatives have to be implemented manually in a computer program. Therefore only a fixed number of terms can be implemented in any given software, which limits the accuracy of the f and g series when the coast time is long. This conflict between the general applicability of the algorithm and programming complexity is not easily resolved with the f and g series approach. For these reasons, the f and g series is replaced by Goodyear's method [17, 18] of orbit determination. This method is similar to the f and g series in that both are Taylor series expansions where all coefficients are functions of the initial state; however, Goodyear's method is an expansion of the state in a regularizing variable ψ introduced below resulting in a completely general solution for both the state and its partial derivatives. This provides an efficient, compact, accurate, and easily implementable solution for all cases of two-body motion. A detailed development of the Goodyear method including all equation derivations can be found in Reference [18], of which a brief overview is reflected below.

6.2 Method Development

6.2.1 Regularizing Transformation

In the absence of thrust the two-body problem can be expressed by the differential equation

$$\ddot{\boldsymbol{r}} = -\frac{\mu}{r^3}\boldsymbol{r} \tag{6.1}$$

where $\boldsymbol{r} \in R^3$ is the position vector expressed in the guidance inertial frame, r is its magnitude, and μ is the Earth's gravitational parameter.

A regularizing transformation is made from t to a new variable ψ defined by the differential equation

$$\dot{\psi} = \frac{1}{r} \tag{6.2}$$

where ψ is zero at the initial time t_0.

In order to simplify derivative expressions to follow, two additional quantities are defined by

$$\sigma = \boldsymbol{r}^T\,\dot{\boldsymbol{r}} \tag{6.3}$$

and

$$\alpha = \dot{\boldsymbol{r}}^T\,\dot{\boldsymbol{r}} - 2\frac{\mu}{r} \tag{6.4}$$

The quantity α has an important property wherein its derivative with respect to ψ results in the following.

$$\alpha' = 2\dot{\boldsymbol{r}}^T\,\dot{\boldsymbol{r}}' + 2\frac{\mu}{r^2}r' \tag{6.5}$$

However, from the differential equation (6.1) above it is seen that

$$\dot{\boldsymbol{r}}' = \ddot{\boldsymbol{r}}t' = -\frac{\mu}{r^2}\boldsymbol{r} \tag{6.6}$$

and therefore

$$\begin{aligned}\alpha' &= -2\dot{\boldsymbol{r}}^T\left(\frac{\mu}{r^2}\boldsymbol{r}\right) + 2\frac{\mu}{r^2}\sigma \\ &= -2\frac{\mu}{r^2}\sigma + 2\frac{\mu}{r^2}\sigma \\ &= 0\end{aligned} \tag{6.7}$$

The quanity α remains constant for every value of ψ. The significance of this property is that it allows all ψ derivatives of t to be written as simple functions of its first two derivatives t' and t''. Similarly, all ψ derivatives of $\boldsymbol{r}$ can be written as simple functions of $\boldsymbol{r}'$ and $\boldsymbol{r}''$. This results in the simplified expressions:

$$t' = r \tag{6.8}$$

$$t'' = \boldsymbol{r}^T \dot{\boldsymbol{r}} = \sigma \tag{6.9}$$

$$t''' = \alpha r + \mu = \alpha t' + \mu \tag{6.10}$$

$$t'''' = \alpha t'' \tag{6.11}$$

$$t''''' = \alpha t''' = \alpha^2 t' + \alpha\mu \tag{6.12}$$

$$t'''''' = \alpha^2 t'' \tag{6.13}$$

$$t''''''' = \alpha^2 t''' = \alpha^3 t' + \alpha^2 \mu \tag{6.14}$$

$$\vdots$$

and

$$\boldsymbol{r}' = \dot{\boldsymbol{r}} r \tag{6.15}$$

$$\boldsymbol{r}'' = -\mu(\boldsymbol{r}/r) + \sigma\dot{\boldsymbol{r}} \tag{6.16}$$

$$\boldsymbol{r}''' = \alpha \boldsymbol{r}' \tag{6.17}$$

$$\boldsymbol{r}'''' = \alpha \boldsymbol{r}'' \tag{6.18}$$

$$\boldsymbol{r}''''' = \alpha \boldsymbol{r}''' = \alpha^2 \boldsymbol{r}' \tag{6.19}$$

$$\boldsymbol{r}'''''' = \alpha^2 \boldsymbol{r}'' \tag{6.20}$$

$$\boldsymbol{r}''''''' = \alpha^2 \boldsymbol{r}''' = \alpha^3 \boldsymbol{r}' \tag{6.21}$$

$$\vdots$$

A further inspection of the results above reveal that all ψ derivatives of both t and $\boldsymbol{r}$ can be

written as functions of $\boldsymbol{r}$, its time derivative $\dot{\boldsymbol{r}}$, and its magnitude r resulting in the following.

$$t' = r \tag{6.22}$$

$$t'' = \sigma \tag{6.23}$$

$$t''' = \alpha r + \mu \tag{6.24}$$

$$t'''' = \alpha\sigma \tag{6.25}$$

$$t''''' = \alpha^2 r + \alpha\mu \tag{6.26}$$

$$t'''''' = \alpha^2\sigma \tag{6.27}$$

$$t''''''' = \alpha^3 r + \alpha^2\mu \tag{6.28}$$

$$\vdots$$

and

$$\boldsymbol{r}' = r\dot{\boldsymbol{r}} \tag{6.29}$$

$$\boldsymbol{r}'' = -\mu(\boldsymbol{r}/r) + \sigma\dot{\boldsymbol{r}} \tag{6.30}$$

$$\boldsymbol{r}''' = \alpha(r\dot{\boldsymbol{r}}) \tag{6.31}$$

$$\boldsymbol{r}'''' = \alpha(-\mu(\boldsymbol{r}/r) + \sigma\dot{\boldsymbol{r}}) \tag{6.32}$$

$$\boldsymbol{r}''''' = \alpha^2(r\dot{\boldsymbol{r}}) \tag{6.33}$$

$$\boldsymbol{r}'''''' = \alpha^2(-\mu(\boldsymbol{r}/r) + \sigma\dot{\boldsymbol{r}}) \tag{6.34}$$

$$\boldsymbol{r}''''''' = \alpha^3(r\dot{\boldsymbol{r}}) \tag{6.35}$$

$$\vdots$$

6.2.2 Series Solution

The above results are used in Taylor series expansions of both t and $\boldsymbol{r}$. Expanding t in terms of the regularizing variable ψ gives

$$t = t_0 + t_0{}'\psi + \frac{1}{2}t_0{}''\psi^2 + \frac{1}{3!}t_0{}'''\psi^3 + \frac{1}{4!}t_0{}''''\psi^4 + \dots \tag{6.36}$$

where t_0, $t_0{}'$, $t_0{}''$, $t_0{}'''$, $t_0{}''''$, $\dots$ are evaluated with the initial position $\boldsymbol{r}_0$, velocity $\dot{\boldsymbol{r}}_0$, and magnitude r_0 at the initial time t_0 using the equations from the previous section. The quantities

σ and α are evaluated using the initial values as well, where σ_0 represents this value. The quantity α was shown previously to take the same value for any value of ψ. Substituting the derivative expressions into equation (6.36) and collecting coefficients of r_0, σ_0, and μ yields the following.

$$\begin{aligned} t = t_0 &+ r_0 \left(\psi + \frac{\alpha}{3!}\psi^3 + \frac{\alpha^2}{5!}\psi^5 + \frac{\alpha^3}{7!}\psi^7 + \dots \right) \\ &+ \sigma_0 \left(\frac{1}{2!}\psi^2 + \frac{\alpha}{4!}\psi^4 + \frac{\alpha^2}{6!}\psi^6 + \frac{\alpha^3}{8!}\psi^8 + \dots \right) \\ &+ \mu \left(\frac{1}{3!}\psi^3 + \frac{\alpha}{5!}\psi^5 + \frac{\alpha^2}{7!}\psi^7 + \frac{\alpha^3}{9!}\psi^9 + \dots \right) \end{aligned} \tag{6.37}$$

which gives the value of t correpsonding to a value of ψ. Similarly, expanding $\boldsymbol{r}$ in terms of the regularizing variable ψ gives

$$\boldsymbol{r} = \boldsymbol{r}_0 + \boldsymbol{r}_0{}'\psi + \frac{1}{2}\boldsymbol{r}_0{}''\psi^2 + \frac{1}{3!}\boldsymbol{r}_0{}'''\psi^3 + \frac{1}{4!}\boldsymbol{r}_0{}''''\psi^4 + \dots \tag{6.38}$$

using the equations from the previous section. Substituting the derivative expressions into equation (6.38) and collecting coefficients of $\boldsymbol{r}_0$ and $\dot{\boldsymbol{r}}_0$ yields the following.

$$\begin{aligned} \boldsymbol{r} = &\boldsymbol{r}_0 \left[1 - \frac{\mu}{r_0} \left(\frac{1}{2!}\psi^2 + \frac{\alpha}{4!}\psi^4 + \frac{\alpha^2}{6!}\psi^6 + \frac{\alpha^3}{8!}\psi^8 + \dots \right) \right] \\ &+ \dot{\boldsymbol{r}}_0 \begin{bmatrix} r_0 \left(\psi + \frac{\alpha}{3!}\psi^3 + \frac{\alpha^2}{5!}\psi^5 + \frac{\alpha^3}{7!}\psi^7 + \dots \right) \\ + \sigma_0 \left(\frac{1}{2!}\psi^2 + \frac{\alpha}{4!}\psi^4 + \frac{\alpha^2}{6!}\psi^6 + \frac{\alpha^3}{8!}\psi^8 + \dots \right) \end{bmatrix} \end{aligned} \tag{6.39}$$

which gives the value of $\boldsymbol{r}$ correpsonding to a value of ψ.

6.2.3 Coordinate Solution

The series solutions above are conveniently expressed by defining transcendental functions of the form

$$s_0 = 1 + \frac{\alpha}{2!}\psi^2 + \frac{\alpha^2}{4!}\psi^4 + \frac{\alpha^3}{6!}\psi^6 + \dots \tag{6.40}$$

$$s_1 = \psi + \frac{\alpha}{3!}\psi^3 + \frac{\alpha^2}{5!}\psi^5 + \frac{\alpha^3}{7!}\psi^7 + \dots \tag{6.41}$$

$$s_2 = \frac{1}{2!}\psi^2 + \frac{\alpha}{4!}\psi^4 + \frac{\alpha^2}{6!}\psi^6 + \frac{\alpha^3}{8!}\psi^8 + \dots \tag{6.42}$$

$$s_3 = \frac{1}{3!}\psi^3 + \frac{\alpha}{5!}\psi^5 + \frac{\alpha^2}{7!}\psi^7 + \frac{\alpha^3}{9!}\psi^9 + \dots \tag{6.43}$$

with corresponding ψ derivatives

$$s_0{}' = \alpha s_1 \tag{6.44}$$

$$s_1{}' = s_0 \tag{6.45}$$

$$s_2{}' = s_1 \tag{6.46}$$

$$s_3{}' = s_2 \tag{6.47}$$

The values of the transcendental functions s_0, s_1, s_2, and s_3, are determined by solving the equation

$$t = t_0 + r_0 s_1 + \sigma_0 s_2 + \mu s_3 \tag{6.48}$$

for ψ from which $r(t - t_0)$ can be found from

$$r = r_0 s_0 + \sigma_0 s_1 + \mu s_3 \tag{6.49}$$

Additionally, the quantities f and g are defined as

$$f = 1 - \mu\, s_2/r_0 \tag{6.50}$$

$$g = (t - t_0) - \mu\, s_3 \tag{6.51}$$

where the corresponding time derivatives are given as

$$\dot{f} = -\mu\, s_1/(r\, r_0) \tag{6.52}$$

$$\dot{g} = 1 - \mu\, s_2/r \tag{6.53}$$

This allows the solution for the final position $\boldsymbol{r}$ and veloicity $\dot{\boldsymbol{r}}$ to be expressed in a compact form given below.

$$\boldsymbol{r} = f\, \boldsymbol{r}_0 + g\, \dot{\boldsymbol{r}}_0 \tag{6.54}$$

$$\dot{\boldsymbol{r}} = \dot{f}\, \boldsymbol{r}_0 + \dot{g}\, \dot{\boldsymbol{r}}_0 \tag{6.55}$$

The solutions above are functions of the initial conditions $\boldsymbol{r}_0$ and $\dot{\boldsymbol{r}}_0$ as well as the gravitational parameter μ and the times t and t_0. The differential relationships $d\boldsymbol{r}$ and $d\dot{\boldsymbol{r}}$ in terms of $d\boldsymbol{r}_0$ and $d\dot{\boldsymbol{r}}_0$ are also important and are found by differentiating the coordinate solution

equations (6.54-6.55) and combining the results after eliminating all differentials other than $d\boldsymbol{r}$, $d\dot{\boldsymbol{r}}$, $d\boldsymbol{r}_0$, $d\dot{\boldsymbol{r}}_0$, $d\mu$, dt, and dt_0. In the launch vehicle application, μ is constant, and therefore $d\mu$ is zero. Also, in the current formulation, t_0 corresponds to the fixed main engine cut-off time and therefore dt_0 is zero. The derivation of the differentials is very involved. This results, however, in compact and completely general expressions given in [18].

CHAPTER 7. TERMINAL CONSTRAINT MULTIPLIER

7.0.4 Introduction

As first mentioned in section (3.4.2), this work adds the flexibility to solve for the Lagrange multiplier $\boldsymbol{\nu}$ directly. Elimination of $\boldsymbol{\nu}$ depends on the specific form of orbital insertion conditions used and may not always be desired, and may not always be possible. It certainly does not lend itself to unanticipated changes in insertion conditions resulting from abort scenarios such as Return to Launch Site (RTLS), Trans-Atlantic Landing (TAL), and Abort to Orbit (ATO). Including $\boldsymbol{\nu}$ in the solution of course increases the number of unknowns and equality constraints, however the added benefit may prove to outweigh an otherwise significantly small savings in computation effort. Additionally, the robustness of the a current algorithm is further improved with the introduction of the Hybrid Dogleg method discussed previously. The unknowns and constraints of the problem are summarized below.

7.1 Equality Constraints

In this formulation, the unknowns in the problem are given as

$$\boldsymbol{z} = (\boldsymbol{\lambda}_0,\, \boldsymbol{\lambda}^+_{MECO},\, \boldsymbol{x}^+_{MECO},\, \tau_{OMS},\, \boldsymbol{\lambda}^+_{OMS},\, \boldsymbol{x}^+_{OMS},\, \tau_f,\, \boldsymbol{\nu}) \in R^{32+k} \tag{7.1}$$

where $\boldsymbol{\nu} \in R^k$. The continuity and switching conditions $\boldsymbol{s}_1 - s_5$ remain unchanged and are listed again below.

$$\boldsymbol{s}_1(\boldsymbol{z}) = \Phi(\tau_{MECO} - \tau_0)\boldsymbol{\lambda}_0 - \boldsymbol{\lambda}^+_{MECO} = 0 \tag{7.2}$$

$$\boldsymbol{s}_2(\boldsymbol{z}) = \Phi(\tau_{MECO} - \tau_0)\boldsymbol{x}_0 + \Gamma(\tau_{MECO})\boldsymbol{I}^0(\tau_{MECO}, \tau_0) - \boldsymbol{x}^+_{MECO} = 0 \tag{7.3}$$

$$\boldsymbol{s}_3(\boldsymbol{z}) = \Phi(\tau_{OMS} - \tau_{MECO})\boldsymbol{\lambda}^+_{MECO} - \boldsymbol{\lambda}^+_{OMS} = 0 \tag{7.4}$$

$$\boldsymbol{s}_4(\boldsymbol{z}) = \boldsymbol{x}_{fg}(\tau_{OMS} - \tau_{MECO}, \boldsymbol{x}^+_{MECO}) - \boldsymbol{x}^+_{OMS} = 0 \tag{7.5}$$

$$s_5(\boldsymbol{z}) = {\boldsymbol{\lambda}^+_{OMS}}^T \boldsymbol{x}^+_{OMS} = 0 \tag{7.6}$$

Theses equations provide 25 constraint equations. The final costate $\boldsymbol{\lambda}_f$ and vehicle state $\boldsymbol{x}_f$ are still given by Eqs. (4.26) and (4.27), however the constraint $\boldsymbol{s}_6$ in Eq. (4.28) is changed. The transversality conditions are no longer manipulated and combined with the orbital insertion conditions. Now both conditions provide independent constraints on the problem and are expressed as

$$\boldsymbol{s}_6(\boldsymbol{z}) = \Psi(\boldsymbol{r}_f, \boldsymbol{V}_f) = 0 \tag{7.7}$$

$$\boldsymbol{s}_7(\boldsymbol{z}) = T_{\boldsymbol{\lambda}}\boldsymbol{\lambda}_f - \left(\frac{\partial \Psi}{\partial \boldsymbol{x}_f}\right)^T \boldsymbol{\nu} = 0 \tag{7.8}$$

where

$$T_{\boldsymbol{\lambda}} = \begin{bmatrix} 0 & 0 & 0 & -\omega & 0 & 0 \\ 0 & 0 & 0 & 0 & -\omega & 0 \\ 0 & 0 & 0 & 0 & 0 & -\omega \\ \omega & 0 & 0 & 0 & 0 & 0 \\ 0 & \omega & 0 & 0 & 0 & 0 \\ 0 & 0 & \omega & 0 & 0 & 0 \end{bmatrix} \tag{7.9}$$

Together Eqs. (7.7) and (7.8) constitute $6 + k$ constraint equations. The final transversality condition on the Hamiltonian remains unchanged and provides the last constraint equation.

$$s_8(\boldsymbol{z}) = H(\tau_f) = 0 \tag{7.10}$$

This optimal ascent problem now becomes a multivariate zero-finding problem of a system of $32 + k$ nonlinear algebraic equations

$$\boldsymbol{s}(\boldsymbol{z}) = 0, \quad \boldsymbol{z} \in R^{32+k} \tag{7.11}$$

where $\boldsymbol{s}(\cdot) = (\boldsymbol{s}_1, \boldsymbol{s}_2, \boldsymbol{s}_3, \boldsymbol{s}_4, s_5, \boldsymbol{s}_6, \boldsymbol{s}_7, s_8) : R^{32+k} \rightarrow R^{32+k}$ is a smooth vector function. As can be seen, the dimension of the system of equations depends on the number or orbital insertion conditions.

CHAPTER 8. TERMINAL MODES AND NECESSARY EQUATIONS

8.1 Introduction

As noted above in section (3.4.2), the orbital insertion conditions are specified in terms of k equality constraints on the final state; however, typical conditions are specified by a defined subset of the six target orbital elements. This chapter will introduce various terminal modes and give their corresponding constraint equations in the form of Eq. (3.12).

For the typical orbital insertion conditions, the terminal constraint multipliers can be eliminated from the problem as mentioned in section (3.4.2). This is accomplished by manipulating the 6 transversality equations (3.13-3.14) into $6 - k$ independent conditions thus eliminating the unknown multiplier vector $\boldsymbol{\nu}$. This process is unique and depends on the specific form of terminal conditions. The current implementation takes this approach and the resulting independent conditions for each mode will be given when available.

This work adds the flexibility to solve for the terminal Lagrange multiplier vector $\boldsymbol{\nu}$ directly. The 6 transversality equations (3.13-3.14) become additional constraint equations for the problem. For identical terminal conditions, this procedure adds k unknowns to the problem with k additional constraint equations; however, this is a more general and flexible approach and may be more favorable as previously mentioned. This chapter will give these additional constraint equations for all terminal modes. This approach is well suited for non typical modes in which the elimination of the multiplier vector $\boldsymbol{\nu}$ is inconvenient, too time consuming, or simply not possible.

Keeping inline with the current algorithm implementation resulting from previous work, it should be noted that in this chapter the final state and costate variable definitions vary slightly

from those in Eq. (4.1) and Eq. (4.3), and are given as

$$\boldsymbol{x}_f = \begin{pmatrix} \boldsymbol{r}_f \\ \boldsymbol{V}_f \end{pmatrix} \tag{8.1}$$

$$\boldsymbol{p}_f = \begin{pmatrix} \boldsymbol{p}_{V_f} \\ \boldsymbol{p}_{r_f} \end{pmatrix} \tag{8.2}$$

8.2 Mode 31

This mode consists of three orbital insertion conditions defined by the desired target orbital element values for the semi-major axis a^*, eccentricity e^*, and inclination i^*. The ascending node, true anomaly, and argument periapsis are considered free. This is a so-called free attachment mode in that the final flight path angle γ_f is unconstrained. However, a typical situation is to force $\gamma_f = 0$ thereby requiring the insertion point be at either the perigee or apogee of the target orbit (See Mode 43/44 below).

A unit vector is constructed that relates the vehicle's final position and velocity to the target orbit inclination. Define a z-axis unit vector in the Earth centered inertial (ECI) frame as

$$\mathbf{1}_{NE} = \begin{bmatrix} 0 \\ 0 \\ 1 \end{bmatrix} \tag{8.3}$$

This vector transformed to the guidance frame is given by

$$\mathbf{1}_{NG} = T_{EG}\,\mathbf{1}_{NE} \tag{8.4}$$

where T_{EG} is the transformation matrix as defined in section (3.2.3).

From orbital mechanics, the magnitude of the required final angular momentum vector of the vehicle at the orbital insertion point is given by

$$h^* = \sqrt{a^*(1 - e^{*2})} \tag{8.5}$$

Using the above expressions, the three orbital insertion conditions $\boldsymbol{\Psi} \in R^3$ can be written as

$$\frac{1}{2}\left(\boldsymbol{r}_f \times \boldsymbol{V}_f\right)^T \left(\boldsymbol{r}_f \times \boldsymbol{V}_f\right) - \frac{1}{2}h^{*2} = 0 \tag{8.6}$$

$$\frac{1}{2}\boldsymbol{V}_f{}^T \boldsymbol{V}_f - \frac{1}{r_f} + \frac{1}{2a^*} = 0 \tag{8.7}$$

$$\mathbf{1}_{NG}{}^T \left(\boldsymbol{r}_f \times \boldsymbol{V}_f\right) - h^* \cos i^* = 0 \tag{8.8}$$

where $r_f = \|\boldsymbol{r}_f\|$.

8.2.1 Manipulated Independent Conditions

The 6 transversality equations (3.13-3.14) are manipulated into 3 independent conditions eliminating the unknown multiplier vector $\boldsymbol{\nu} \in R^3$. After much algebraic manipulation this results in the conditions

$$\left(\boldsymbol{h}_f{}^T \boldsymbol{p}_{r_f}\right)\left[\boldsymbol{h}_f{}^T \left(\boldsymbol{r}_f \times \mathbf{1}_{NG}\right)\right] + \left(\boldsymbol{h}_f{}^T \boldsymbol{p}_{V_f}\right)\left[\boldsymbol{h}_f{}^T \left(\boldsymbol{V}_f \times \mathbf{1}_{NG}\right)\right] = 0 \tag{8.9}$$

$$r_f{}^3 \boldsymbol{V}_f{}^T \boldsymbol{p}_{r_f} - \boldsymbol{r}_f{}^T \boldsymbol{p}_{V_f} = 0 \tag{8.10}$$

$$\boldsymbol{p}_{r_f}{}^T \left(\boldsymbol{r}_f \times \boldsymbol{V}_N\right)\left(\boldsymbol{r}_f \times \boldsymbol{h}_f\right)^T \left(\boldsymbol{V}_f \times \boldsymbol{r}_N\right) + \boldsymbol{p}_{V_f}{}^T \left(\boldsymbol{V}_f \times \boldsymbol{r}_N\right)\left(\boldsymbol{V}_f \times \boldsymbol{h}_f\right)^T \left(\boldsymbol{r}_f \times \boldsymbol{V}_N\right) = 0 \tag{8.11}$$

where $\boldsymbol{h}_f = \boldsymbol{r}_f \times \boldsymbol{V}_f$ is the angular momentum vector, $\boldsymbol{r}_N = \boldsymbol{r}_f \times \mathbf{1}_{NG}$, and $\boldsymbol{V}_N = \boldsymbol{V}_f \times \mathbf{1}_{NG}$.

8.2.2 Additional Transversality Conditions

The 6 transversality conditons (3.13-3.14) involving the Lagrange multipler $\boldsymbol{\nu} \in R^3$ are given by

$$\boldsymbol{p}_{r_f} - \left(\boldsymbol{V}_f \times \boldsymbol{h}_f\right)\nu_1 - \frac{1}{r_f{}^3}\boldsymbol{r}_f \nu_2 - \left(\boldsymbol{V}_f \times \mathbf{1}_{NG}\right)\nu_3 = 0 \tag{8.12}$$

$$\boldsymbol{p}_{V_f} + \left(\boldsymbol{r}_f \times \boldsymbol{h}_f\right)\nu_1 - \boldsymbol{V}_f \nu_2 + \left(\boldsymbol{r}_f \times \mathbf{1}_{NG}\right)\nu_3 = 0 \tag{8.13}$$

8.3 Mode 41

Mode 41 consists of four orbital insertion conditions defined by the desired target orbital element values for the semi-major axis a^*, eccentricity e^*, inclination i^*, and ascending node Ω^*.

The true anomaly and argument periapsis are considered free. This is also a free attachment mode in that the final flight path angle γ_f is unconstrained allowing the insertion point to be located at any point on the target orbit.

A unit angular momentum vector of the desired target orbital plane is constructed from the target inclination and ascending node. This vector, defined in the ECI frame is given as

$$\mathbf{1}_{HE} = \begin{bmatrix} \sin\Omega^* \sin i^* \\ -\cos\Omega^* \sin i^* \\ \cos i^* \end{bmatrix} \tag{8.14}$$

This vector transformed to the guidance frame is given by

$$\mathbf{1}_{HG} = T_{EG}\, \mathbf{1}_{HE} \tag{8.15}$$

where T_{EG} is the transformation matrix as defined in section (3.2.3).

Again, the magnitude of the required final angular momentum vector of the vehicle at the orbital insertion point is given by

$$h^* = \sqrt{a^*(1 - e^{*2})} \tag{8.16}$$

Using the above expressions, the four orbital insertion conditions $\boldsymbol{\Psi} \in R^4$ can be written as

$$\boldsymbol{r}_f \times \boldsymbol{V}_f - \boldsymbol{h}_f{}^* = 0 \quad \in R^3 \tag{8.17}$$

$$\frac{1}{2}\boldsymbol{V}_f{}^T \boldsymbol{V}_f - \frac{1}{r_f} + \frac{1}{2a^*} = 0 \tag{8.18}$$

where $r_f = \|\boldsymbol{r}_f\|$ and $\boldsymbol{h}_f{}^* = h^* \mathbf{1}_{HG}$

8.3.1 Manipulated Independent Conditions

The 6 transversality equations (3.13-3.14) are manipulated into 2 independent conditions eliminating the unknown multiplier vector $\boldsymbol{\nu} \in R^4$. After much algebraic manipulation this results in the conditions

$$\boldsymbol{p}_{r_f}{}^T \boldsymbol{V}_f - \frac{1}{{r_f}^3} \boldsymbol{p}_{V_f}{}^T \boldsymbol{r}_f = 0 \tag{8.19}$$

$$\boldsymbol{p}_{r_f}{}^T (\boldsymbol{r}_f \times \boldsymbol{h}_f{}^*) + \boldsymbol{p}_{V_f}{}^T (\boldsymbol{V}_f \times \boldsymbol{h}_f{}^*) = 0 \tag{8.20}$$

8.3.2 Additional Transversality Conditions

The 6 transversality conditons (3.13-3.14) involving the Lagrange multipler $\boldsymbol{\nu} \in R^4$ are given by

$$\boldsymbol{p}_{r_f} + \text{skew}\,(\boldsymbol{V}_f) \begin{bmatrix} \nu_1 \\ \nu_2 \\ \nu_3 \end{bmatrix} - \frac{1}{{r_f}^3} \boldsymbol{r}_f \nu_4 = 0 \tag{8.21}$$

$$\boldsymbol{p}_{V_f} - \text{skew}\,(\boldsymbol{r}_f) \begin{bmatrix} \nu_1 \\ \nu_2 \\ \nu_3 \end{bmatrix} - \boldsymbol{V}_f \nu_4 = 0 \tag{8.22}$$

8.4 Mode 43/44

This mode involves four orbital insertion constraints defined by the desired target orbital element values for the semi-major axis a^*, eccentricity e^* inclination, i^*, and a final flight path angle γ_f, which is set to zero. Therefore the insertion point is at the perigee or apogee of the target orbit and the final dimensionless position and velocity are given by

$$r_f^* = a^*(1 - e^*) \tag{8.23}$$

$$V_f^* = \sqrt{\frac{1 + e^*}{a^*(1 - e^*)}} \tag{8.24}$$

for the perigee and

$$r_f^* = a^*(1 + e^*) \tag{8.25}$$

$$V_f^* = \sqrt{\frac{1 - e^*}{a^*(1 + e^*)}} \tag{8.26}$$

for the apogee.

A unit vector is constructed that relates the vehicle's final position and velocity to the target orbit inclination. Define a z-axis unit vector in the ECI frame as

$$\mathbf{1}_{NE} = \begin{bmatrix} 0 \\ 0 \\ 1 \end{bmatrix} \tag{8.27}$$

This vector transformed to the guidance frame is given by

$$\mathbf{1}_{NG} = T_{EG}\,\mathbf{1}_{NE} \tag{8.28}$$

where T_{EG} is the transformation matrix as defined in section (3.2.3).

Using the above expressions, the four orbital insertion conditions $\mathbf{\Psi} \in R^4$ can be written as

$$\frac{1}{2}\boldsymbol{r}_f{}^T\boldsymbol{r}_f - \frac{1}{2}r_f^{*2} = 0 \tag{8.29}$$

$$\frac{1}{2}\boldsymbol{V}_f{}^T\boldsymbol{V}_f - \frac{1}{2}V_f^{*2} = 0 \tag{8.30}$$

$$\mathbf{1}_{NG}{}^T\left(\boldsymbol{r}_f \times \boldsymbol{V}_f\right) - r_f^* V_f^* \cos i^* = 0 \tag{8.31}$$

$$\boldsymbol{r}_f{}^T\boldsymbol{V}_f = 0 \tag{8.32}$$

8.4.1 Manipulated Independent Conditions

Substituting Ψ into Eqs. (3.13-3.14) results in 6 transversality conditions. Performing strategic dot and cross product operations on these conditions enables the elimination of the multiplier vector $\boldsymbol{\nu} \in R^4$. This results in 2 additional independent constraint equations given by

$$\boldsymbol{V}_f{}^T\boldsymbol{p}_{r_f}r_f^{*2} - \boldsymbol{r}_f{}^T\boldsymbol{p}_{V_f}V_f^{*2} = 0 \tag{8.33}$$

$$\begin{aligned}\left[\left(\boldsymbol{r}_f \times \boldsymbol{V}_f\right)^T\boldsymbol{p}_{r_f}\right]\left[\left(\boldsymbol{r}_f \times \boldsymbol{V}_f\right)^T\left(\boldsymbol{r}_f \times \mathbf{1}_{NG}\right)\right] \\ + \left[\left(\boldsymbol{r}_f \times \boldsymbol{V}_f\right)^T\boldsymbol{p}_{V_f}\right]\left[\left(\boldsymbol{r}_f \times \boldsymbol{V}_f\right)^T\left(\boldsymbol{V}_f \times \mathbf{1}_{NG}\right)\right] = 0\end{aligned} \tag{8.34}$$

8.4.2 Additional Transversality Conditions

The 6 transversality conditons (3.13-3.14) involving the Lagrange multipler $\boldsymbol{\nu} \in R^4$ are given by

$$\boldsymbol{p}_{r_f} - \boldsymbol{r}_f\nu_1 - \left(\boldsymbol{V}_f \times \mathbf{1}_{NG}\right)\nu_3 - \boldsymbol{V}_f\nu_4 = 0 \tag{8.35}$$

$$\boldsymbol{p}_{V_f} - \boldsymbol{V}_f\nu_2 + \left(\boldsymbol{r}_f \times \mathbf{1}_{NG}\right)\nu_3 - \boldsymbol{r}_f\nu_4 = 0 \tag{8.36}$$

8.5 Mode 46

This mode involves four insertion conditions defined by the desired final position magnitude r_f^*, velocity magnitude V_f^*, inclination i^*, and flight path angle γ_f^*.

Again, a unit vector is constructed that relates the vehicle's final position and velocity to the desired inclination. Define a z-axis unit vector in the ECI frame as

$$\mathbf{1}_{NE} = \begin{bmatrix} 0 \\ 0 \\ 1 \end{bmatrix} \tag{8.37}$$

This vector transformed to the guidance frame is given by

$$\mathbf{1}_{NG} = T_{EG}\,\mathbf{1}_{NE} \tag{8.38}$$

where T_{EG} is the transformation matrix as defined in section (3.2.3).

The four resulting insertion conditions can be written as

$$\frac{1}{2}\boldsymbol{r}_f{}^T\boldsymbol{r}_f - \frac{1}{2}r_f^{*2} = 0 \tag{8.39}$$

$$\frac{1}{2}\boldsymbol{V}_f{}^T\boldsymbol{V}_f - \frac{1}{2}V_f^{*2} = 0 \tag{8.40}$$

$$\mathbf{1}_{NG}{}^T\left(\boldsymbol{r}_f \times \boldsymbol{V}_f\right) - r_f^* V_f^* \cos\gamma_f^* \cos i^* = 0 \tag{8.41}$$

$$\boldsymbol{r}_f{}^T\boldsymbol{V}_f - r_f^* V_f^* \sin\gamma_f^* = 0 \tag{8.42}$$

8.5.1 Manipulated Independent Conditions

Substituting Ψ into Eqs. (3.13-3.14) results in 6 transversality conditions. Elimination of the multiplier vector $\boldsymbol{\nu} \in R^4$ results in 2 additional independent constraint equation given by

$$\left(\boldsymbol{V}_f{}^T\boldsymbol{p}_{r_f}\right) r_f^* - \left(\boldsymbol{r}_f{}^T\boldsymbol{p}_{V_f}\right) V_f^* + r_f^* V_f^* \sin\gamma_f^* \left[\boldsymbol{V}_f{}^T\boldsymbol{p}_{V_f} - \boldsymbol{r}_f{}^T\boldsymbol{p}_{r_f}\right] = 0 \tag{8.43}$$

$$\left(\boldsymbol{h}_f{}^T\boldsymbol{p}_{r_f}\right)\left(\boldsymbol{h}_f{}^T\boldsymbol{r}_N\right) + \left(\boldsymbol{h}_f{}^T\boldsymbol{p}_{V_f}\right)\left(\boldsymbol{h}_f{}^T\boldsymbol{V}_N\right) = 0 \tag{8.44}$$

where $\boldsymbol{h}_f = \boldsymbol{r}_f \times \boldsymbol{V}_f$ is the angular momentum vector, $\boldsymbol{r}_N = \boldsymbol{r}_f \times \mathbf{1}_{NG}$, and $\boldsymbol{V}_N = \boldsymbol{V}_f \times \mathbf{1}_{NG}$.

8.5.2 Additional Transversality Conditions

The 6 transversality conditions (3.13-3.14) involving the Lagrange multiplier $\boldsymbol{\nu} \in R^4$ are given by

$$\boldsymbol{p}_{r_f} - \boldsymbol{r}_f \nu_1 - (\boldsymbol{V}_f \times \mathbf{1}_{NG})\,\nu_3 - \boldsymbol{V}_f \nu_4 = 0 \tag{8.45}$$

$$\boldsymbol{p}_{V_f} - \boldsymbol{V}_f \nu_2 + (\boldsymbol{r}_f \times \mathbf{1}_{NG})\,\nu_3 - \boldsymbol{r}_f \nu_4 = 0 \tag{8.46}$$

8.6 Mode 51

Mode 51 consists of five orbital insertion conditions defined by the desired target orbital element values for the semi-major axis a^*, eccentricity e^*, inclination i^*, ascending node Ω^*, and and a final flight path angle γ_f, which is set to zero. The true anomaly and argument of the periapsis are considered free. The insertion point is at the perigee or apogee of the target orbit and the final position and velocity are given again as

$$r_f^* = a^*(1 - e^*) \tag{8.47}$$

$$V_f^* = \sqrt{\frac{1 + e^*}{a^*(1 - e^*)}} \tag{8.48}$$

for the perigee and

$$r_f^* = a^*(1 + e^*) \tag{8.49}$$

$$V_f^* = \sqrt{\frac{1 - e^*}{a^*(1 + e^*)}} \tag{8.50}$$

for the apogee. As was done for mode 41, a unit angular momentum vector of the desired target orbital plane is constructed from the target inclination and ascending node and is given as

$$\mathbf{1}_{HE} = \begin{bmatrix} \sin\Omega^* \sin i^* \\ -\cos\Omega^* \sin i^* \\ \cos i^* \end{bmatrix} \tag{8.51}$$

This vector transformed to the guidance frame is given by

$$\mathbf{1}_{HG} = T_{EG}\,\mathbf{1}_{HE} \tag{8.52}$$

where T_{EG} is the transformation matrix as defined in section (3.2.3).

Again, the magnitude of the required final angular momentum vector of the vehicle at the orbital insertion point is given by

$$h^* = \sqrt{a^*(1 - e^{*2})} \tag{8.53}$$

Using the above expressions, the five orbital insertion conditions $\boldsymbol{\Psi} \in R^5$ can be written as

$$\frac{1}{2}\boldsymbol{r}_f{}^T\boldsymbol{r}_f - \frac{1}{2}r_f^{*2} = 0 \tag{8.54}$$

$$\frac{1}{2}\boldsymbol{V}_f{}^T\boldsymbol{V}_f - \frac{1}{2}V_f^{*2} = 0 \tag{8.55}$$

$$\boldsymbol{r}_f{}^T\boldsymbol{V}_f = 0 \tag{8.56}$$

$$\boldsymbol{r}_f{}^T\mathbf{1}_{HG} = 0 \tag{8.57}$$

$$\boldsymbol{V}_f{}^T\mathbf{1}_{HG} = 0 \tag{8.58}$$

8.6.1 Manipulated Independent Conditions

Substituting Ψ into Eqs. (3.13-3.14) results in 6 transversality conditions. Elimination of the multiplier vector $\boldsymbol{\nu} \in R^5$ results in 1 additional independent constraint equation given by

$$\left(\boldsymbol{V}_f{}^T\boldsymbol{p}_{r_f}\right)r_f^{*2} - \left(\boldsymbol{r}_f{}^T\boldsymbol{p}_{V_f}\right)V_f^{*2} = 0 \tag{8.59}$$

8.6.2 Additional Transversality Conditions

The 6 transversality conditions (3.13-3.14) involving the Lagrange multiplier $\boldsymbol{\nu} \in R^5$ are given by

$$\boldsymbol{p}_{r_f} - \boldsymbol{r}_f\nu_1 - \boldsymbol{V}_f\nu_3 - \mathbf{1}_{HG}\nu_4 = 0 \tag{8.60}$$

$$\boldsymbol{p}_{V_f} - \boldsymbol{V}_f\nu_2 - \boldsymbol{r}_f\nu_3 - \mathbf{1}_{HG}\nu_5 = 0 \tag{8.61}$$

CHAPTER 9. VARIABLE FIRST BURN

9.1 Introduction

Replacing the modified Newton-Raphson method with Powell's hybrid dogleg method, replacing the f and g series in orbital mechanics with the more general Goodyear's method for coast state propagation, and adding the flexibility of solving for the terminal constraint Lagrange multipliers directly are all aimed at increasing the robustness and capability of the current analytical multiple-shooting burn-coast-burn optimal ascent guidance algorithm. Powell's hybrid dogleg method is a more robust numerical non-linear equation solver in the general sense and increases both the convergence reliability and rate in the burn-coast-burn application. The use of a regularizing transformation variable discussed in the development of Goodyear's method in chapter (6) allows for a completely general solution of the two-body problem and its easy implementation provides enhanced performance over the more traditional f and g series. Adding the flexibility to solve for the terminal constraint Lagrange multipliers directly allows the algorithm to handle non typical orbital insertion conditions and eliminates the need to analytically manipulate each unique set of orbital insertion conditions in order to remove the multipliers from the problem.

Each of the additions and enhancements to the current analytical multiple-shooting burn-coast-burn optimal ascent guidance algorithm are implemented on the current framework wherein the first burn is of fixed duration determined by available propellant. This lends itself to two stage vehicle configurations where a main booster vehicle is jettisoned after exhausting its propellant supply. An orbital vehicle would then begin an optimized coast before turning on its engines and maneuvering itself into the desired target orbit. This framework can be expanded to include any number of optimized burn / coast sequences as mentioned in

section (3.1). This chapter will develop the necessary equations enabling this generality. In the context of the burn-coast-burn sequence presented in this work, the first burn is no longer of fixed duration and the resulting necessary conditions are given. Such a sequence could be optimized for a single stage vehicle.

9.2 Development

First introduced in section (3.4.3) and rewritten below for convenience, the Hamiltonian is given as

$$H = \boldsymbol{p}_r{}^T \boldsymbol{V} - \omega^2 \boldsymbol{p}_V{}^T \boldsymbol{r} + T\left(\frac{\boldsymbol{p}_V{}^T \mathbf{1}_T}{mg_0} - \frac{p_m}{c} - \frac{1}{c}\right) := H_{NT} + TS \tag{9.1}$$

where H_{NT} is the portion of the Hamiltonian having no thrust influence. The optimal control problem must satisfy the optimality condition (2.10) wherein the thrust direction unit vector $\mathbf{1}_T$ is chosen to maximize the Hamiltonian (9.1) for optimal values of the state and costate requiring alignment with the costate vector $\boldsymbol{p}_V$, or $\mathbf{1}_T = \boldsymbol{p}_V / \|\boldsymbol{p}_V\|$. The Hamiltonian can be then be written as

$$H = \boldsymbol{p}_r{}^T \boldsymbol{V} - \omega^2 \boldsymbol{p}_V{}^T \boldsymbol{r} + T\left(\frac{\|\boldsymbol{p}_V\|}{mg_0} - \frac{p_m}{c} - \frac{1}{c}\right) := H_{NT} + TS \tag{9.2}$$

In addition, the switching function S determines the vehicle thrust pattern according to the rule

$$T = \begin{cases} T_{max} & \text{if } S > 0, \\ 0 & \text{if } S < 0. \end{cases} \tag{9.3}$$

For the launch vehicle vacuum ascent problem, it was seen that Hamiltonian remains constant along an optimal trajectory, and further, is is identically equal to zero.

$$H(\tau_f) = 0, \quad \tau_0 \leq \tau \leq \tau_f \tag{9.4}$$

At each interior thrust on/off switching point τ_i, $S = 0$, and therefore $H_{NT} = 0$. However, applying the condition $H_{NT} = 0$ at multiple switching points is not sufficient as H_{NT} itself remains identically zero along coast arcs.

For a completely general set of terminal constraints, the term H_{NT} at the final time τ_f can be non-zero. One approach at determining the interior switching point necessary conditions is

to initialize the switching function at the first free switching point τ_1 using equation (9.4) [13].

$$S(\tau_1) = -\frac{H_{NT}(\tau_1)}{T} \tag{9.5}$$

If the following switching point τ_2 corresponds to the end of a coast arc, then the second switching condition is given by

$$S(\tau_2) = S(\tau_1) + [S(\tau_2) - S(\tau_1)] = S(\tau_1) + \frac{\|\boldsymbol{p}_V(\tau_2)\| - \|\boldsymbol{p}_V(\tau_1)\|}{mg_0} \tag{9.6}$$

using the fact that the vehicle mass and mass costate are constant along a coast arc. If the following switching condition corresponds to the end of a burn arc, then the second switching condition is given by

$$S(\tau_2) = S(\tau_1) + \frac{H_{NT}(\tau_1) - H_{NT}(\tau_2)}{T} \tag{9.7}$$

again using the fact that the Hamiltonian is identically zero on a burn arc. The switching functions can be calculated using this approach resulting in the interior point necessary conditions

$$S(\tau_i) = 0, \quad i = 1, 2, \ldots, n \tag{9.8}$$

where n is the number of free switching points.

For typical terminal constraints such as those in chapter (8), it can be seen that in the absence of thrust the condition $H_{NT}(\tau_f) = 0$ is automatically satisfied [30]. This allows the interior point necessary conditions to be expressed in a simplified form as

$$\|\boldsymbol{p}_V(\tau_i)\| - \|\boldsymbol{p}_V(\tau_{i-1})\| = 0, , \quad i = 1, 2, \ldots, n, \quad \text{across a coast arc} \tag{9.9}$$

$$H_{NT}(\tau_{i+1}) - H_{NT}(\tau_i) = 0, \quad i = 1, 2, \ldots, n, \quad \text{across a burn arc} \tag{9.10}$$

Both approaches determine the interior switching point necessary conditions without needing to numerically integrate the mass costate p_m.

9.3 Burn Coast Burn Implementation

In the current framework it was necessary that $S(\tau_{OMS}) = 0$, or alternatively $H_{NT}(\tau_{OMS}) = 0$. This provided the only necessary condition in determining the optimal switching time τ_{OMS}.

Expanding the framework to allow the first burn to be of variable duration requires the addition of a switching condition at τ_{MECO} where the first burn ends and the coast begins. This condition is determined from equation (9.9) and is given simply as

$$\|\boldsymbol{p}_V(\tau_{OMS})\| - \|\boldsymbol{p}_V(\tau_{MECO})\| = 0 \tag{9.11}$$

Recalling the multiple shooting formulation discussed in section (4.3), nodes are placed at τ_{MECO} and τ_{OMS}. At each node, propagated and guessed primer vector solutions can be written as $\boldsymbol{p}_V^-(\tau_{MECO})$, $\boldsymbol{p}_V^+(\tau_{MECO})$, $\boldsymbol{p}_V^-(\tau_{OMS})$, and $\boldsymbol{p}_V^+(\tau_{OMS})$ where the - and + represent propagated and guessed respectively. Refer to figure (4.1). Unlike the propagated solutions, the guessed solutions $\boldsymbol{p}_V^+(\tau_{MECO})$ and $\boldsymbol{p}_V^+(\tau_{OMS})$ are independent and therefore writing equation (9.11) as

$$\|\boldsymbol{p}_V^+(\tau_{OMS})\| - \|\boldsymbol{p}_V^+(\tau_{MECO})\| = 0 \tag{9.12}$$

or alternatively

$$\frac{1}{2}\boldsymbol{p}_V^+(\tau_{OMS})^T\boldsymbol{p}_V^+(\tau_{OMS}) - \frac{1}{2}\boldsymbol{p}_V^+(\tau_{MECO})^T\boldsymbol{p}_V^+(\tau_{MECO}) = 0 \tag{9.13}$$

decreases the implementation complexity as the Jacobian computation is greatly simplified.

CHAPTER 10. VERIFICATION AND VALIDATION METHODS

10.1 Introduction

The multiple shooting formulation approach and the numerical methods presented above for the launch vehicle vacuum ascent trajectory optimization problem must be verified to ensure the accuracy of the optimal trajectories found. Two methods are adopted to accomplish this task. An industry standard aerospace trajectory optimization software, Optimal Trajectories by Implicit Simulation (OTIS) [19, 20, 21], is used as another but very different method of solving the burn-coast-burn sequence optimization problem under identical conditions. Additionally, the approach presented above is verified using closed-loop simulated trajectories. A series of test cases for the terminal modes presented above is performed and results presented. The test cases are specifically chosen to allow comparisons among the modes and to emphasize desired characteristics of the optimized trajectories and consequences resulting from a given modes constraint enforcement. The two verification methods are briefly discussed below.

10.2 Closed-Loop Verification

Closed-loop simulations provide an ultimate check for the validity of the open-loop solution determined by analytical multiple shooting formulation above. In closed-loop simulations, the optimization problem utilizing the analytical multiple shooting approach is solved in every Δt seconds (known as the guidance cycle) using the current condition as the initial condition. A new optimal ascent solution is generated from the vechicle's current state to the orbital insertion point. The trajectory is simulated by numerically integrating the vehicle dynamics in Eqs. (3.4-3.5) with an inverse-square gravity field. The thrust direction and throttle commands are from from the optimal solution just found. If the closed-loop trajectory closely matches

the open-loop solution, the validity of the algorithm is verified.

10.3 OTIS Verification

10.3.1 Briefing and Capabilities

The Optimal Trajectories by Implicit Simulation (OTIS) [19, 20, 21] program is a general purpose program used to perform trajectory performance studies. OTIS contains no embedded vehicle specific aerodynamic or propulsion models and therefore allows the user to simulate a wide variety of vehicles including launch vehicles. OTIS can be used to analyze multi-vehicle problems, such as a multi-stage launch system with a fly back booster; where trajectories are generated for all elements of the launch stack including the fly back of the booster. Trajectory generation, targeting and optimization can all be accomplished using OTIS. The default non-linear optimization package used in solving problems with OTIS is SLSQP and is included with OTIS. However, as the problems become more complex, such as the launch vehicle vacuum ascent trajectory optimization problem, CPU times will become excessively large. Another optimizer, SNOPT [22], developed at Standard University can be used with OTIS. SNOPT is a sparse optimizer and OTIS lends itself well to sparse optimization techniques. SNOPT is available as a package that must be obtained seperately from OTIS. SNOPT is the nonlinear optimization package utilized for this study.

To accommodate the trajectory optimization procedure, the trajectory is divided into sub arcs called phases linked together by events. During each phase, the number of vehicle states, controls, path constraints, and vehicle definition remain unchanged. Targeting information is then specified at the events. Discontinuities such as time, control, and certain state variables are allowed to occur at the events. The linking of phases is accomplished with either linear or nonlinear constraints and how they are linked defines a complete trajectory. OTIS allows for seven different phase types.

1. **A** **A**nalytic propagation

2. **E** **E**xplicit integration

3. **I** **I**mplicit integration

4. **P** **P**seudo-Spectral integration

5. **J** **J**ump phase

6. **S** **S**tate transformation

7. **T** **T**ransformation of coordinates

The launch vehicle optimal vacuum ascent problem uses both the implicit integration (I) and jump (J) phases of OTIS. The fundamental idea behind implicit integration is to form a representation of the system states along the trajectory and then enforce constraints such that the representation agrees with the equations of motion for a finite number of nodes along the trajectory while also satisfying any path constraints and boundary conditions. For the launch vehicle optimal vacuum ascent problem, vehicle states and controls become independent parameters in the optimization problem. A representation is shown below in Figure (10.1). OTIS implements four types of implicit integration: collocation, quadrature, nodal general

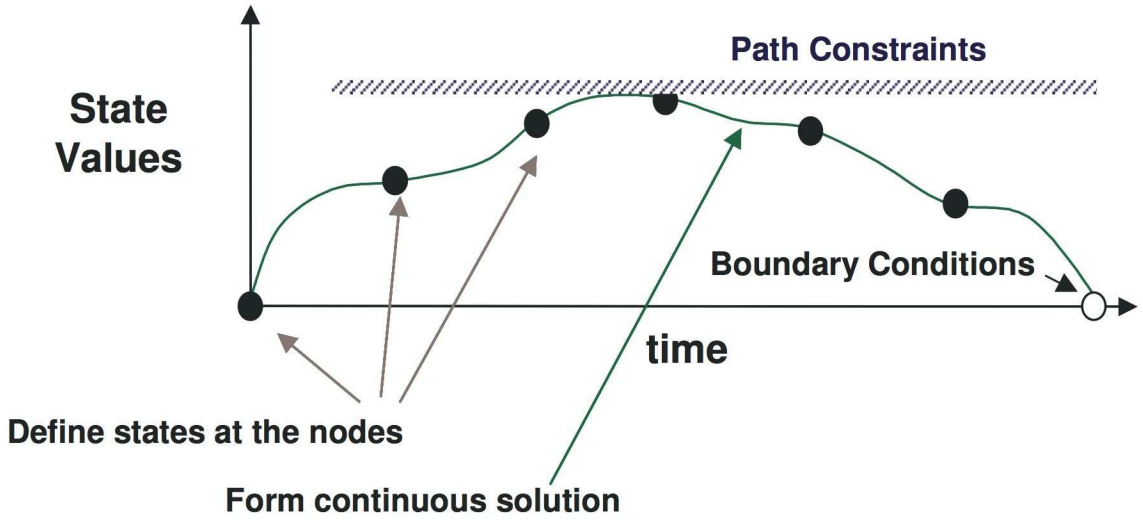

Figure 10.1 Implicit Integration [20]

defects, and segment level general defects.

The primary implicit integration method adopted for the launch vehicle optimal vacuum ascent problem is collocation. The vehicles equations of motion are evaluated using state

and control estimates at "cardinal nodes" along the trajectory to provide time derivatives at these nodes. Using both these states and corresponding time derivatives, a polynomial representation of the vehicle states is created using Hermite interpolation. This polynomial representation is then used to evaluate the vehicle states at nodes interior to the cardinal nodes. At these interior nodes, time derivatives are evaluated both from differentiation of the polynomial representation and also from direct evaluation of the vehicles equations of motion. The objective of the collocation procedure is to then drive the difference between these two time derivatives, or "defects", at the interior nodes to zero. This procedure can be visualized below in Figure (10.2).

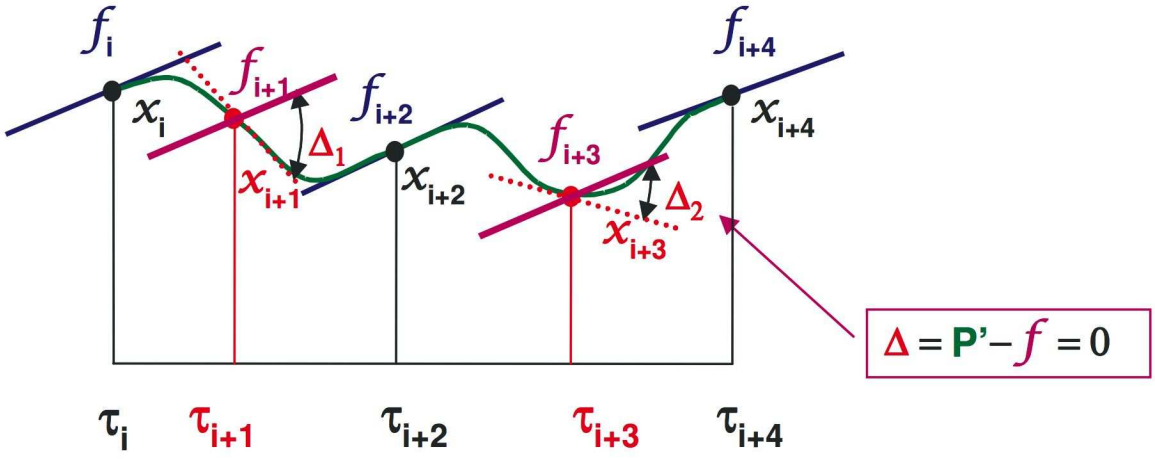

Figure 10.2 Collocation Defects [20]

10.3.2 Burn-Coast-Burn Application

The implementation of OTIS to solve the launch vehicle optimal vacuum ascent problem is described below. As mentioned previously, OTIS divides the trajectory into multiple phases. For the launch vehicle optimal vacuum ascent problem of concern, the trajectory is divided into four phases.

The first phase of the trajectory, as mentioned previously, is a continuation of the endo-atmospheric flight and begins just after the launch vehicle clears the atmosphere and consists of a "Super-X-33" vehicle with a X-37 vehicle piggy-backed. Necessary vehicle information

is given in the next chapter. This phase continues until all the X-33's propellant burns off and is referred to as main engine cut-off (MECO). Therefore this phase is of fixed time and depends on the vehicles total mass and its propellant mass flow rate. This is an implicit integration (I) phase with the inertial roll, pitch, and yaw angles as the independent controls. The information required by OTIS to fully define this phase includes the vehicle's propulsion model; initial and final coordinates, control values, mass values and time estimates; and any boundary constraints. A final boundary constraint on the vehicle's mass is specified for this phase which will fix the phase time. OTIS uses the Earth Centered Inertial (ECI) frame whereas the analytical multiple-shooting formulation uses the Guidance or Plumbline Inertial frame. A simple coordinate transformation will suffice, however it should be noted that OTIS requires a specific Julian date offset guaranteeing the ECI frame x-axis alignment with 0° longitude.

The second phase of the trajectory is a Jump (J) phase wherein the the empty weight of the X-33 vehicle is jettisoned from the X-37; and hence this phase does not require any independent controls or propulsion models. The information required by OTIS to define this phase includes initial and final coordinate guesses, mass values, and times; as well as a jump deletion parameter specifying the amount of weight to be jettisoned from the current stacked configuration. This phase results in essentially a zero length phase with a very large reduction in vehicle weight.

The X-37 will begin a time optimized unpowered coast arc before maneuvering into the specified orbit during the last powered phase. This coast arc is the third phase of trajectory and, being unpowered, does not required any independent controls or propulsion models. Again, the information required by OTIS to define this phase includes initial and final coordinate guesses, vehicle mass, and time estimates. This is an implicit integration (I) phase using the collocation method where the initial state of the vehicle fully defines its trajectory during the unpowered coast.

Upon completion of the optimized coast, the X-37 begins the trajectory's second powered stage, or Orbital Maneuver System (OMS) burn, into the desired orbit satisfying all orbital

insertion conditions. This is an implicit integration (I) phase with the inertial roll, pitch, and yaw angles as the independent controls. The information required by OTIS to fully define this phase includes the vehicle's propulsion model; initial and final coordinates, control values, mass values and time estimates; and any boundary constraints. The final boundary constraints specified will depend on the desired target orbit and will typically be a subset of the six target orbital elements.

The optimization objective in OTIS is specified by desired parameters to be optimized and their corresponding phases of optimization. For the launch vehicle optimal vacuum ascent problem, the optimization parameter is the final weight of the last powered stage in phase four.

CHAPTER 11. RESULTS

11.1 Launch Configuration

The two stage vehicle configuration discussed previously is used for the verification of the AMS method for the burn-coast-burn vacuum ascent trajectory optimization problem and consists of a "super X-33" reusable launch vehicle with a piggy-backed X-37 orbital vehicle. All necessary data for these vehicles are shown below.

Data required for the X-33 reusable launch vehicle are given below in Table (11.1).

Table 11.1 X-33 Data

Thrust (vac)	2,303,000 N
I_{sp} (vac)	711.395 sec
Empty Weight	37,557 kg

Data required for the X-37 orbital vehicle are given below in Table (11.2).

Table 11.2 X-37 Data

Thrust (vac)	29,269 N
I_{sp} (vac)	330 sec
Empty Weight	1,270 kg
Propellant Weight	3,628.74 kg
Payload Weight	544.31 kg

The launch site for all test cases shown below is at Kennedy Space Center (KSC), (longitude=$-80.85°$, latitude $28.29°$). This information is necessary in establishing the guidance inertial frame for the launch as well as the required guidance to ECI coordinate transformation. The computation of the optimal first stage ascent trajectory through the atmosphere is divided into two segments: the endo-atmospheric portion and the exo-atmospheric portion,

separated at a given altitude around 90 km resulting in a mass of approximately 70,0000 kg. The exo-atmospheric portion of the first stage is the first vacuum burn of the analytical multiple-shooting problem formulation and the second burn the second stage of the launch vehicle. The endo-atmospheric solution is obtained from methodology outlined in References 14 and 15. For different target orbital insertion conditions, the optimal endo-atmospheric solutions results in somewhat different exo-atmospheric ascent initial conditions necessary for the AMS method, however, in this study the same exo-atmospheric ascent initial conditions are used for all test cases.

11.2 Mode 31 / 43 Comparisons

As mentioned previously, mode 31 consists of three orbital insertion conditions defined by the desired target orbital element values for the semi-major axis a^*, eccentricity e^*, and inclination i^*. This is a free attachment mode in that the final flight path angle γ_f is not constrained. Mode 43 requires the same orbital insertion conditions as mode 31 in addition to constraining the final flight path angle to zero such that the insertion point is the perigee of the target orbit. A set of test cases with target orbital insertion conditions as well as an identical set for mode 43 including the final $\gamma_f = 0$ constraint is given below in Table 11.3 . In addition, three circular target orbits for Mode 43 are listed.

Table 11.3 Mode 31 & 43 Target Orbits

Case	Mode	perigee alt. (km)	e	i (deg)	γ_f (deg)
1	31	300	0.1	51.6	Free
2	31	500	0.1	51.6	Free
3	31	1000	0.1	51.6	Free
4	31	300	0.3	51.6	Free
5	31	500	0.3	51.6	Free
6	31	1000	0.3	51.6	Free
7	31	500	0.1	28.5	Free
8	31	500	0.3	28.5	Free
9	43	300	0.1	51.6	0.0
10	43	500	0.1	51.6	0.0
11	43	1000	0.1	51.6	0.0
12	43	300	0.3	51.6	0.0
13	43	500	0.3	51.6	0.0
14	43	1000	0.3	51.6	0.0
15	43	500	0.1	28.5	0.0
16	43	500	0.3	28.5	0.0
17	43	1000	0.0	51.6	0.0
18	43	500	0.0	51.6	0.0
19	43	500	0.0	51.6	0.0

Results for mode 31 and 43 test cases in Table 11.3 are listed in Tables 11.4 and 11.5, respectively. Recalling that the burn time of the first vacuum burn is fixed and determined from propellant availability, the difference in converged second burn time directly translates into the difference in deliverable payload mass, or vehicle performance. Both the second vacuum burn time and mass are listed for convenience. In terms of vehicle performance, all methods match quite closely and is very noteworthy in that OTIS is a direct approach using collocation, a very different method than the indirect AMS method that finds the trajectory based on optimal control necessary conditions. Further, the extent to which the open-loop AMS trajectory matches the full non-linear gravity closed-loop simulation driven by a current condition open-loop AMS solution at each guidance cycle is reassuring. The small differences in the open-loop AMS solution and the converged closed-loop simulation is to be expected and results from approximations made in the Analytical Multiple-Shooting problem formulation such as the linear gravity approximation and thrust quadrature approximations for each burn. During the coast phase the launch vehicle is trading kinetic energy for potential energy. The higher the orbital insertion altitude, the longer the coast arc tends to be, and the more critical

is its length to the performance of the vehicle. Figures 11.1 and 11.2 show the closed-loop altitude and velocity profiles along with their corresponding body axis pitch and yaw angle time histories with respect to the guidance frame (see Fig 3.2) defined with a 2-3-1 rotation sequence. The small yaw angles in figure 11.2 are due to the fact that the launch azimuth is oriented in the direction defined by the target orbit inclination so as to minimize the yaw maneuvers, a common practice in launch vehicle guidance. Some cases were found where, depending on insertion conditions, higher altitudes did not always translate to a longer coast arc, however, the presence of the optimized coast arc remains very significant to vehicle performance.

The performance index on the final mass in the optimal burn-coast-burn problem appears to be fairly insensitive to the coast time. Indeed, significant differences in the converged coast time between OTIS and the AMS method does not result in significant differences in orbital insertion mass. This disagreement in optimal coast times becomes much more noticeable for higher altitude orbital insertions. The two methods do, however, find similar solutions for the lower altitude orbits. These results are illustrated in Figures 11.3 and 11.4, which show the altitude and velocity profiles for both OTIS and the closed-loop AMS simulation for cases 2 and 3. The small changes in insertion mass even for disproportionately large changes in coast time results in a "flat optimum" and it was found that direct methods such as OTIS tend to converge to different solutions, most notably in the converged coast time, depending on initial guess inputs. The AMS method, an indirect method, did not suffer from this problem and was consistently able to converge to the same solution for the same case for large changes in the initial guess.

An important comparison between all mode 31 and the respective mode 43 test cases is seen from the value of the true anomaly at insertion. Mode 43 requires the insertion point be the perigee of the resulting target orbit, which evident from the table is not always the optimal insertion point. This result is consistent with both the AMS method and OTIS. This is exemplified by test case 6 and 14 which results in a difference in second burn time of approximately 5 seconds equating to a deliverable payload difference of 45.25 kg, a substantial

difference assuming payload mass of 500 kg. Figures 11.5 and 11.6 show the optimized ascent trajectory and insertion target orbit for case 6. This illustrates the non-perigee optimal insertion point and shows the true anomaly at insertion. Figure 11.6 is viewed in the direction of the target orbit angular momentum vector allowing this to be seen easily.

Table 11.4 Mode 31 Results

Case	Method	Coast (sec)	2^{nd} Burn (sec)	Final Mass (kg)	True Anomaly (deg)
1	OTIS	24.6240	334.0512	2421.7212	7.43432
	AMS	20.0371	334.3829	2416.8352	0.00000
	AMS closed-loop	26.4927	331.7147	2438.4000	6.21815
2	OTIS	135.2167	345.9007	2314.5505	11.41668
	AMS	126.1379	346.8496	2304.0113	0.00000
	AMS closed-loop	134.5228	343.6698	2329.8000	11.13721
3	OTIS	293.8752	389.6641	1918.7385	10.29114
	AMS	226.0024	390.5117	1908.8694	0.00000
	AMS closed-loop	243.9442	388.0392	1922.5500	12.08240
4	OTIS	54.2115	386.7927	1944.7088	2.38447
	AMS	43.9989	386.6586	1943.7401	0.00000
	AMS closed-loop	53.1648	384.5900	1958.7500	1.29348
5	OTIS	152.4945	395.3354	1867.4451	6.08704
	AMS	132.0432	396.0864	1858.4179	0.00000
	AMS closed-loop	142.8387	393.3418	1877.3000	6.75834
6	OTIS	257.3082	427.3834	1577.5918	11.21645
	AMS	207.8629	429.6897	1554.3082	0.00000
	AMS closed-loop	226.6251	425.4743	1587.7000	12.72862
7	OTIS	129.0704	345.5416	2317.7982	12.07388
	AMS	129.1712	345.9306	2312.3279	0.00000
	AMS closed-loop	137.6387	342.7682	2338.8500	10.95298
8	OTIS	126.4071	394.4810	1875.1728	8.65202
	AMS	135.5817	395.3242	1865.3161	0.00000
	AMS closed-loop	146.4793	392.5993	1886.3500	6.55688

Table 11.5 Mode 43 Results

Case	Method	Coast (sec)	2^{nd} Burn (sec)	Final Mass (kg)	True Anomaly (deg)
9	OTIS	34.1034	334.7211	2415.6628	0.00000
	AMS	18.1730	334.3978	2416.6999	0.00001
	AMS closed-loop	26.7410	331.8191	2438.4000	0.00688
10	OTIS	159.6698	346.2189	2311.6721	0.00000
	AMS	120.9575	346.9562	2303.0468	0.00000
	AMS closed-loop	130.6213	344.5979	2320.7500	0.05877
11	OTIS	307.5751	390.7985	1908.4785	0.00000
	AMS	219.6417	390.9169	1905.2019	0.00001
	AMS closed-loop	238.4151	390.0967	1904.4500	0.33734
12	OTIS	36.9882	387.9814	1933.9577	0.00000
	AMS	35.0215	386.7056	1943.3146	0.00000
	AMS closed-loop	50.0246	384.6953	1958.7500	0.01839
13	OTIS	166.2501	396.8354	1853.8786	0.00000
	AMS	112.2931	396.3527	1856.0081	0.00000
	AMS closed-loop	126.6136	394.5985	1868.2500	0.01075
14	OTIS	293.3618	431.1413	1543.6039	0.00000
	AMS	187.5651	430.6763	1545.3795	0.00000
	AMS closed-loop	206.4970	430.4641	1542.4500	0.06999
15	OTIS	170.3501	348.4420	2291.5658	0.00000
	AMS	106.7140	350.5581	2270.4490	0.41001
	AMS closed-loop	128.8965	346.3061	2302.6500	0.11132
16	OTIS	172.6211	397.0370	1852.0556	0.00000
	AMS	115.9672	395.5898	1862.9119	0.00000
	AMS closed-loop	130.4734	393.7107	1877.3000	0.08649
17	OTIS	27.7985	302.1463	2710.2808	N/A
	AMS	21.4543	301.3659	2715.6387	N/A
	AMS closed-loop	26.5988	298.4510	2737.0500	N/A
18	OTIS	174.1365	315.1391	2592.7694	N/A
	AMS	132.5598	315.9119	2583.9970	N/A
	AMS closed-loop	139.9287	313.4425	2601.3000	N/A
19	OTIS	319.0053	366.0883	2131.9660	N/A
	AMS	240.3386	365.9951	2130.7439	N/A
	AMS closed-loop	258.0000	365.2223	2130.7000	N/A

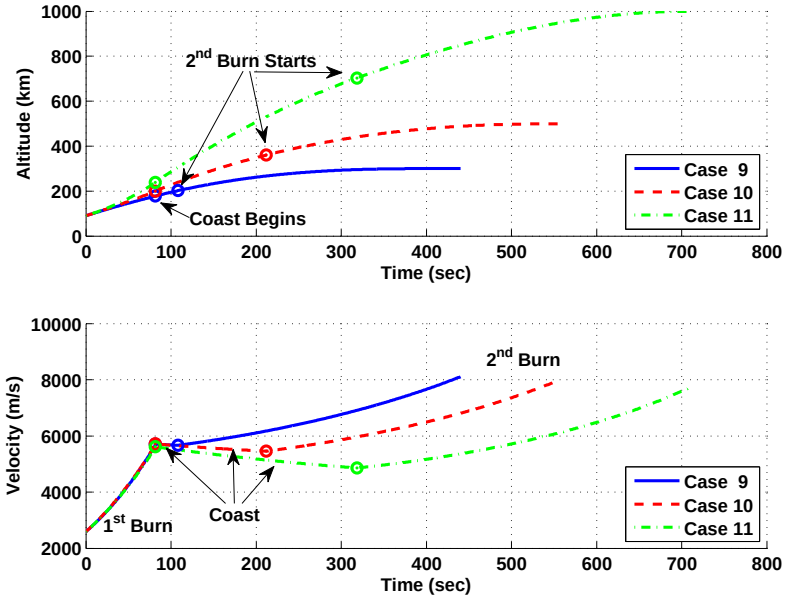

Figure 11.1 Altitude and velocity profiles of the AMS closed-loop burn–coast-burn ascent trajectories for cases 9-11

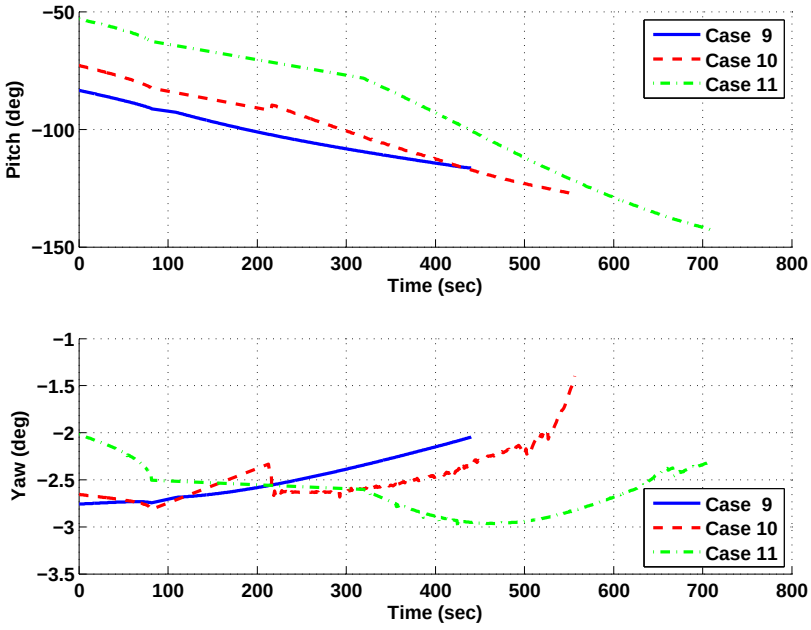

Figure 11.2 Pitch and yaw angles along the AMS closed-loop burn–coast-burn ascent trajectories with respect to the launch plumbline (guidance) frame for cases 9-11

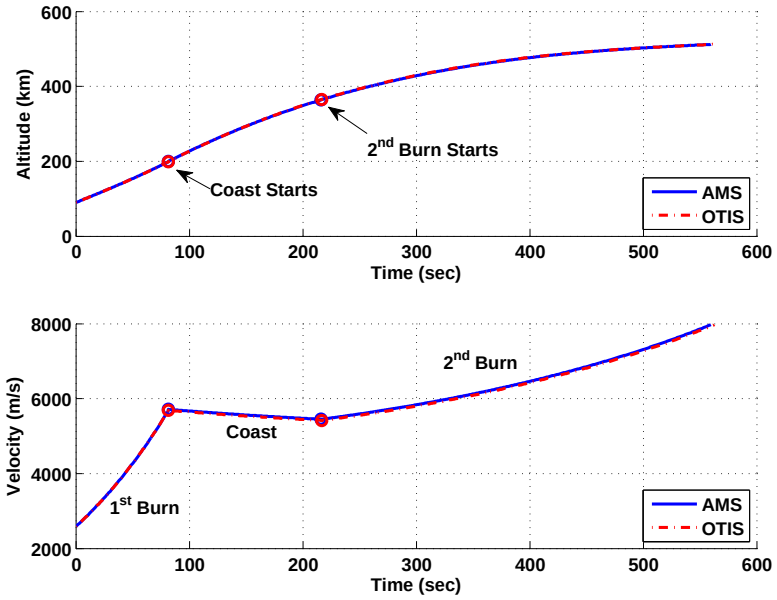

Figure 11.3 AMS and OTIS altitude and velocity comparison for case 2

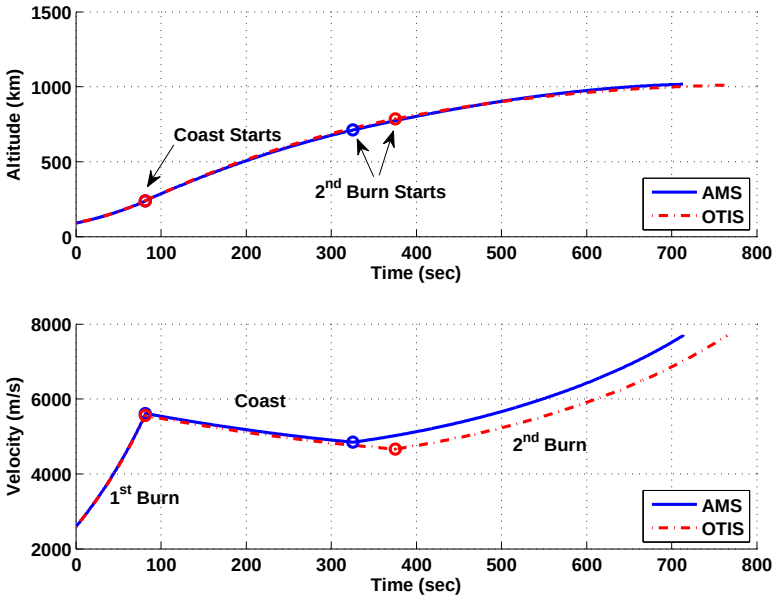

Figure 11.4 AMS and OTIS altitude and velocity comparison for case 3

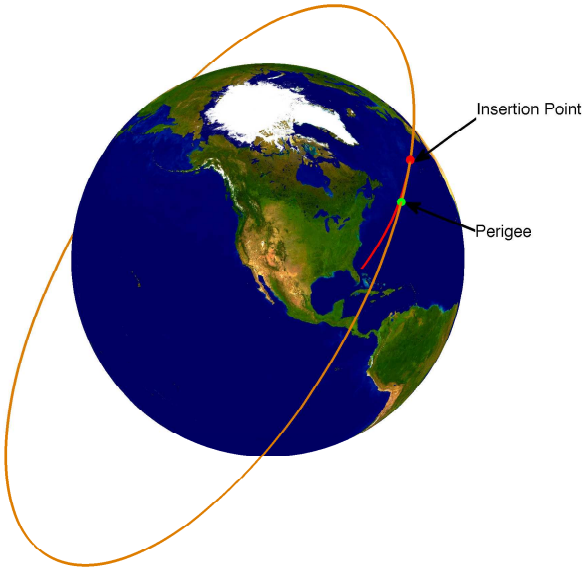

Figure 11.5 AMS closed-loop ascent trajectory and target insertion orbit for case 6

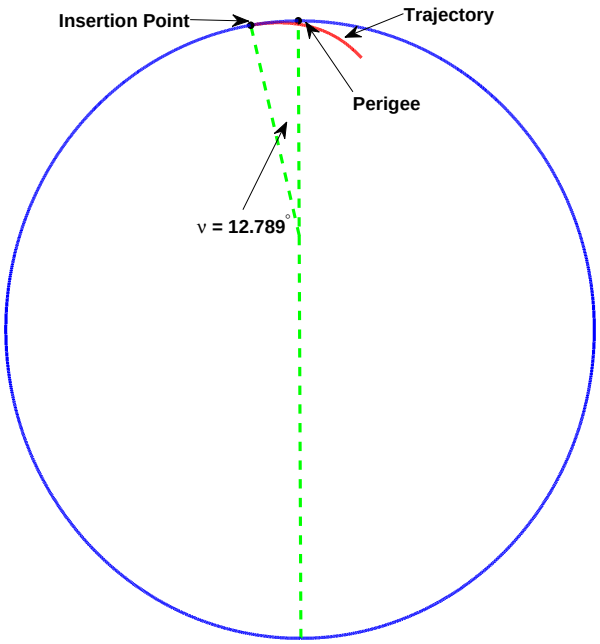

Figure 11.6 AMS closed-loop ascent trajectory and target insertion orbit illustrating true anomaly at insertion for case 6

11.3 Mode 41 / 51 Comparisons

Mode 41 consists of four orbital insertion conditions defined by the desired target orbital element values for the semi-major axis a^*, eccentricity e^*, inclination i^*, and ascending node Ω^*. This is a free attachment mode in that the final flight path angle γ_f is not constrained. Mode 51 requires the same orbital insertion conditions as mode 41 in addition to constraining the final flight path angle to zero such that the insertion point is the perigee of the target orbit. Modes 41 and 51 are similar to modes 31 and 43 respectively and differ only from the additional constraint on the ascending node. This fixes the target orbital plane leaving the only unknown the location of the perigee on the orbit. A set of test cases with target orbital insertion conditions as well as an identical set for mode 51 including the final $\gamma_f = 0$ constraint is given below in Table 11.6 . In addition, three circular target orbits for Mode 51 are listed. This set of test cases is identical to those of 31 and 43 with the addition of a fixed ascending node Ω^*. It should be noted that for the initial conditions used for all test cases in this work, target orbits with unconstrained ascending nodes converge to approximately 255° for inclinations of 51.6° and 185° for inclinations of 28.5°.

Table 11.6 Mode 41 & 51 Target Orbits

Case	Mode	perigee alt. (km)	e	i (deg)	γ_f (deg)	Ω (deg)
20	41	300	0.1	51.6	Free	250
21	41	500	0.1	51.6	Free	250
22	41	1000	0.1	51.6	Free	250
23	41	300	0.3	51.6	Free	250
24	41	500	0.3	51.6	Free	250
25	41	1000	0.3	51.6	Free	250
26	41	500	0.1	28.5	Free	180
27	41	500	0.3	28.5	Free	180
28	51	300	0.1	51.6	0.0	250
29	51	500	0.1	51.6	0.0	250
30	51	1000	0.1	51.6	0.0	250
31	51	300	0.3	51.6	0.0	250
32	51	500	0.3	51.6	0.0	250
33	51	1000	0.3	51.6	0.0	250
34	51	500	0.1	28.5	0.0	180
35	51	500	0.3	28.5	0.0	180
36	51	1000	0.0	51.6	0.0	250
37	51	500	0.0	51.6	0.0	250
38	51	500	0.0	51.6	0.0	250

Results for mode 41 and 51 test cases in Table 11.6 are listed in Tables 11.7 and 11.8, respectively. Again, both the second vacuum burn time and mass are listed for convenience. In terms of vehicle performance, all methods match quite closely as was the case for modes 31 and 43. The open-loop AMS trajectory continues to match the full non-linear gravity AMS closed-loop simulation which is evidence the AMS method has no problem handling the additional constraint on the problem. For modes 31 and 43 it was seen that for higher orbital insertion altitudes, the longer the coast arc tends to be, and the more critical is its length to the performance of the vehicle. This trend is again seen for mode 51 wherein the insertion point must be the perigee of the target orbit. However, from the results in Table 11.7, longer coast arcs for higher insertion altitudes is not the typical outcome for mode 41. This is explained by the variation of optimal insertion points found in terms of the true anomaly at insertion in addition to the unconstrained target orbit perigee direction which can be much different from the corresponding mode 51 cases.

The ascending node constraint enforced in modes 41 and 51 appears to be the dominate constraint. Enforcing the ascending node constraint Ω in addition to the semi-major axis a, eccentricity e, and inclination i fully defines the target orbital plane leaving the only unknown the perigee direction. It can be seen from Table 11.6 that the target orbit ascending node for modes 41 and 51 are set at approximately a 5° offset from their natural unconstrained converged values for the initial conditions used in this work. Enforcing this constraint has a very noticeable impact on vehicle performance. Every mode 41 and 51 case results in a significantly lower final mass than the corresponding mode 31 and 43 case as shown in Tables 11.7 and 11.8. Constraining the ascending node to the values in Table 11.6 forces the launch vehicle to make substantial out of plane maneuvers during ascent to align itself with the target orbital plane. These out of plane maneuvers require longer second burn times causing a significant decrease in final vehicle mass at insertion. For modes 31 and 43 it was shown (see Fig. 11.2) that the yaw angle is generally very small during the ascent due to the initial launch azimuth direction. Expensive out of plane maneuvers result in much larger yaw angles during the ascent as illustrated in Figure 11.8 with a comparison of case 33 and corresponding

case 14. Figure 11.7 shows the altitude and velocity profiles for these cases. As seen in the figures, both cases have very similar velocity and altitude profiles. In case 33, however, the large yawing motion during the ascent results in a longer second burn time by approximately 7 seconds translating into a final mass reduction of approximately 63 kg. Further verifying these results, Figures 11.9 and 11.10 show two views of the optimized trajectory and target insertion orbit for mode 41 test case 25. Again, easily seen from the figures, the launch vehicle performs substantial yawing maneuvers to align and insert itself into the desired target orbit. These results are consistent for both the AMS method and OTIS.

Similar to modes 31 and 43, the performance index on the final mass in the optimal burn-coast-burn problem continues to be fairly insensitive to the coast time. Significant differences in the converged coast time between OTIS and the AMS method does not result in significant differences in orbital insertion mass. This disagreement in optimal coast times is again more noticeable for higher altitude orbital insertions. The small changes in insertion mass for disproportionately large changes in coast time is in part due to the "flat optimum" characteristics of the optimal ascent problem as mentioned previously. Further understanding of the terminal mode constraints can help explain this "flat optimum" most often resulting in optimal coast time disagreement between the AMS and OTIS methods. Is is to be noted and understood that the desired target orbits are not fully defined. Mode 41 and 51 does fix the target orbital plane as mentioned, but does not constrain the perigee location. Given this, for any test case the AMS and OTIS methods may not insert into the same orbit and in general they will not, however, both satisfy the terminal constraints at insertion. This freedom helps explain why both methods can agree in terms of vehicle performance even with substantial disagreement in optimal coast time. This can be demonstrated by analyzing a mode 51 case wherein the orbital plane and insertion point on the orbit are fixed. Figure 11.11 shows the AMS and OTIS trajectories and insertion orbits for mode 51 case 33. Both insertions must be at the perigee of the target orbit, and from Table 11.8, it is seen that the optimized coast arc for the OTIS trajectory is substantially longer that that found by the AMS method. For this reason, it is expected that the OTIS insertion point be somewhat downrange of the AMS insertion

and indeed this is the result. Figure 11.12 illustrates the "flat optimum" characteristic of the problem, again for case 33, by sweeping the coast time over a 200 second window bracketing the original converged coast times found by both the OTIS and AMS methods. As can be seen from figure, the variation in final burn time is very insensitive to the coast duration in this range. Discussed above, the only remaining unconstrained orbital insertion parameter is the argument of perigee, the variation of which is also shown in the figure. Easily seen from the figure, increasing the coast time simply pushes the perigee direction and insertion point further downrange from the launch site, and visa versa.

In regards to the solutions obtained from OTIS, a few comments should be noted. In many cases, adjusting the guessed final burn time values was required to obtain the optimal solution found. Further change of these values could prevent OTIS from retrieving the same solution, or in some situations even a similar solution. It was observed that adjusting the coast and or final burn time bounds would additionally have a significant impact on the converged solution. This prevented obtaining a sweep solution simply by adjusting the coast time duration while leaving all other parameters unchanged. In addition, scaling of problem parameters highly influenced convergence rates and final solutions. It is recognized that OTIS is a very general trajectory optimization software allowing for much user configuration, hence and a more complete knowledge of its proper use in regards to this specific problem may have relieved some of these issues.

Table 11.7 Mode 41 Results

Case	Method	Coast (sec)	2^{nd} Burn (sec)	Final Mass (kg)	True Anomaly (deg)
20	OTIS	259.9649	351.9201	2260.1084	28.88764
	AMS	219.0324	352.1562	2255.9867	20.38100
	AMS closed-loop	231.6762	349.9753	2275.5000	19.04381
21	OTIS	270.9058	361.7805	2170.9273	11.64281
	AMS	191.2724	363.3863	2154.3536	0.98688
	AMS closed-loop	204.5619	364.9046	2139.7500	1.61218
22	OTIS	299.9342	398.2460	1841.1204	8.97000
	AMS	211.8645	401.6461	1808.1027	10.88184
	AMS closed-loop	227.6674	400.0388	1813.9500	12.15001
23	OTIS	265.5381	399.2454	1832.0815	10.57011
	AMS	210.3717	397.9093	1841.9211	6.07592
	AMS closed-loop	227.1023	396.1889	1850.1500	5.03092
24	OTIS	222.2749	407.0645	1761.3633	2.34400
	AMS	158.6010	407.3729	1756.2756	3.49641
	AMS closed-loop	174.9292	404.9382	1777.7500	4.93180
25	OTIS	285.9631	442.5412	1440.4989	11.85391
	AMS	149.9988	438.8672	1471.2519	11.49603
	AMS closed-loop	164.2296	436.9191	1488.1500	14.74207
26	OTIS	130.6578	345.4328	2318.7820	12.48016
	AMS	88.9099	346.4386	2307.7307	12.04604
	AMS closed-loop	94.3723	343.9121	2329.8000	15.26107
27	OTIS	219.2165	396.1688	1859.9077	0.00000
	AMS	15.7832	396.0942	1858.3475	12.37148
	AMS closed-loop	21.0860	393.6329	1877.3000	16.89375

Table 11.8 Mode 51 Results

Case	Method	Coast (sec)	2^{nd} Burn (sec)	Final Mass (kg)	True Anomaly (deg)
28	OTIS	188.2341	356.1665	2221.7026	0.23231
	AMS	168.6447	356.3202	2218.3019	0.00000
	AMS closed-loop	177.0205	354.2091	2230.2500	0.16114
29	OTIS	228.3949	366.3698	2129.4199	0.22885
	AMS	188.8833	363.5015	2153.3116	0.00001
	AMS closed-loop	198.4591	361.0573	2166.9000	0.01260
30	OTIS	326.8909	398.5508	1838.3637	0.22111
	AMS	230.6249	401.1288	1812.7843	0.00001
	AMS closed-loop	248.3052	399.9408	1823.0000	0.02116
31	OTIS	182.9739	399.9333	1825.8598	0.19379
	AMS	170.6421	399.4623	1827.8661	0.00000
	AMS closed-loop	182.1409	397.6953	1841.1000	0.03067
32	OTIS	235.0993	405.9083	1771.8204	0.14380
	AMS	180.8982	405.2135	1761.5226	0.00000
	AMS closed-loop	193.6338	404.8655	1777.7500	0.00441
33	OTIS	317.0431	438.8030	1474.3089	0.13850
	AMS	201.6559	437.9284	1479.7483	0.00000
	AMS closed-loop	220.8111	437.2554	1479.1000	0.09196
34	OTIS	151.4102	347.6747	2298.5052	0.22882
	AMS	122.5030	346.2990	2308.9943	0.00000
	AMS closed-loop	132.1887	343.9411	2329.8000	0.00545
35	OTIS	158.9689	397.0465	1851.9692	0.14366
	AMS	114.0376	395.8322	1860.7183	0.00000
	AMS closed-loop	128.4066	394.1371	1868.2500	0.00323
36	OTIS	200.4568	330.3483	2455.2113	N/A
	AMS	171.1778	330.8833	2448.5065	N/A
	AMS closed-loop	178.0483	328.7342	2465.5500	N/A
37	OTIS	159.8574	339.3094	2374.1639	N/A
	AMS	196.6761	337.2291	2391.0771	N/A
	AMS closed-loop	204.6825	334.6980	2411.2500	N/A
38	OTIS	337.8690	380.0354	2005.8236	N/A
	AMS	248.9145	378.2907	2019.4688	N/A
	AMS closed-loop	265.7263	377.1271	2022.1000	N/A

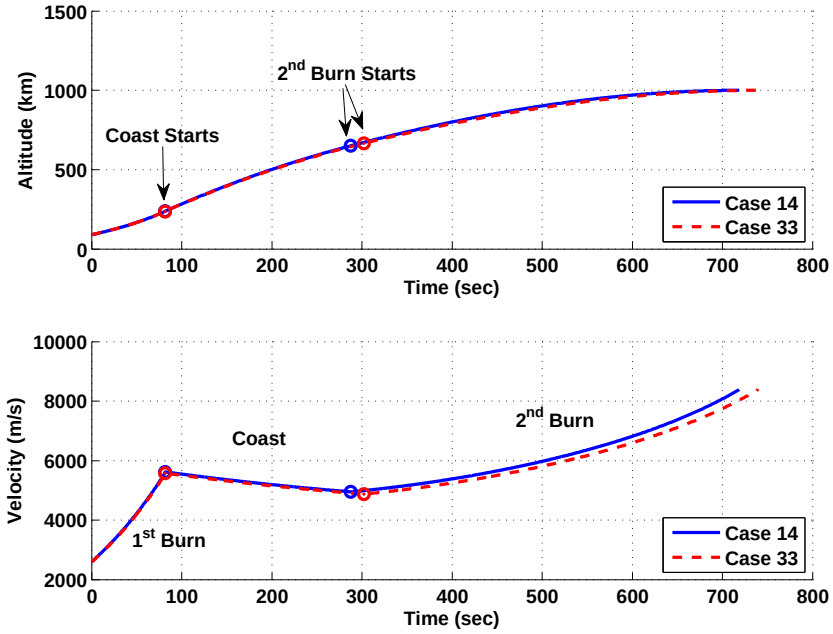

Figure 11.7 Altitude and velocity profiles of the AMS closed-loop burn–coast-burn ascent trajectories for cases 14 and 33

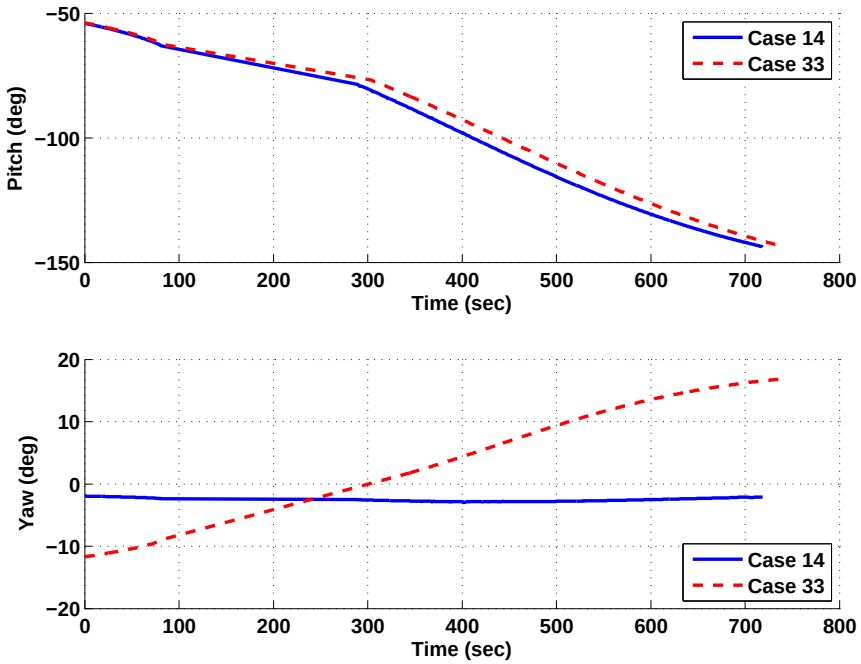

Figure 11.8 Pitch and yaw angles along the AMS closed-loop burn–coast-burn ascent trajectories with respect to the launch plumbline (guidance) frame for cases 14 and 33

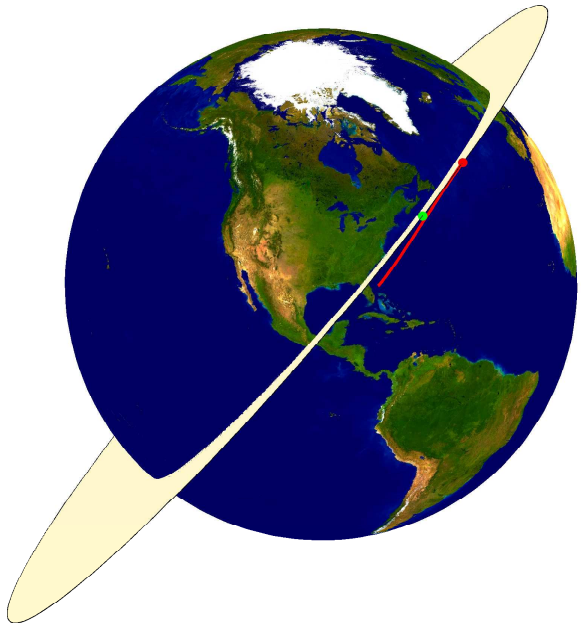

Figure 11.9 View 1: AMS closed-loop ascent trajectory and target insertion orbit for case 25 illustrating large out of plane motion (orbit shading for visual convenience)

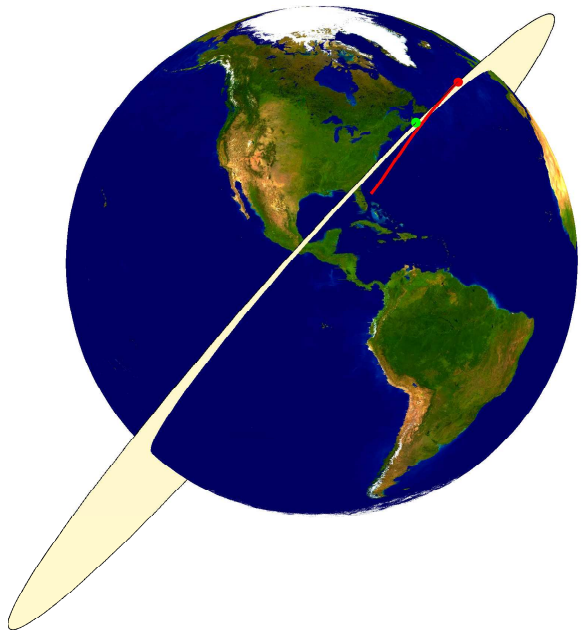

Figure 11.10 View 2: AMS closed-loop ascent trajectory and target insertion orbit for case 25 illustrating large out of plane motion (orbit shading for visual convenience)

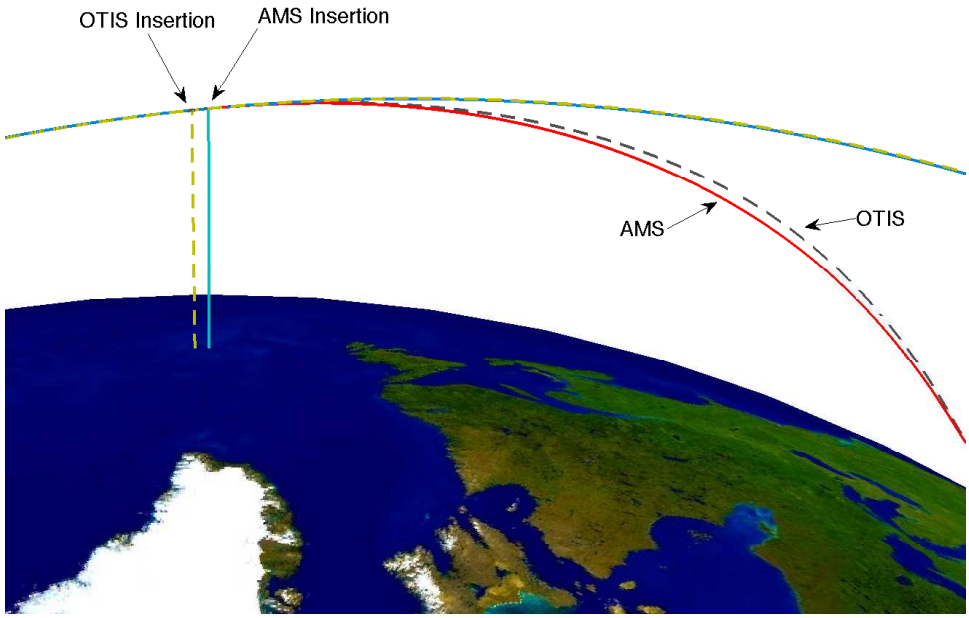

Figure 11.11 AMS closed-loop and OTIS ascent trajectories and orbital insertion perigee direction for case 33

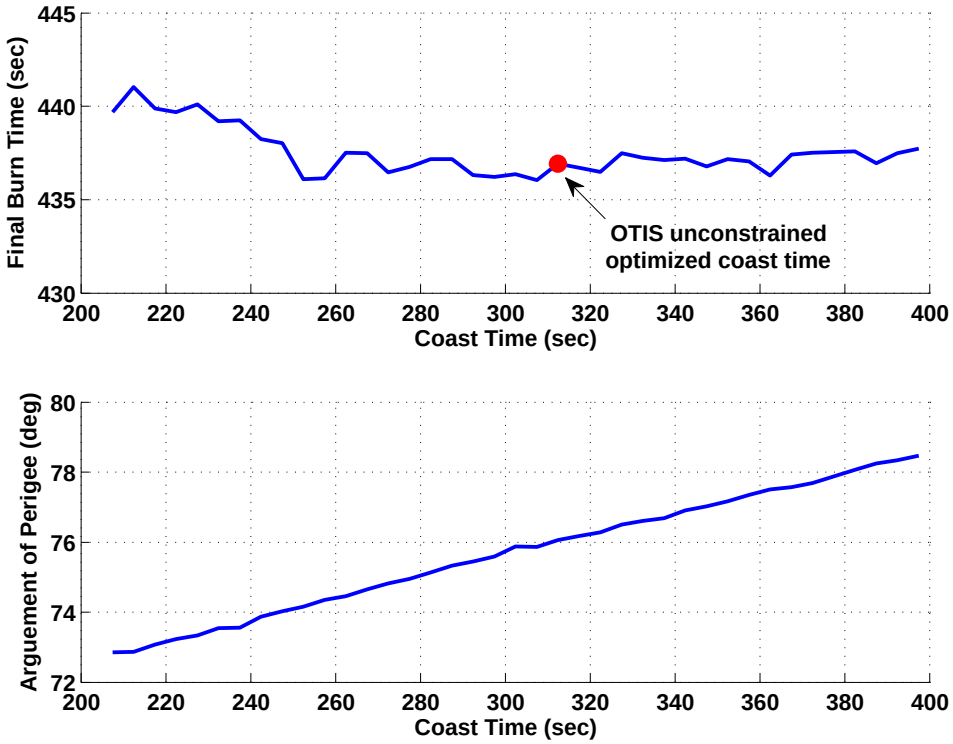

Figure 11.12 OTIS coast time sweep for case 33

11.4 Mode 46 Results

Mode 46 involves four insertion conditions defined by the desired final position magnitude r_f^*, velocity magnitude V_f^*, inclination i^*, and flight path angle γ_f^*. This mode is unlike the others in that it is not defined from typical orbital elements and the conditions need not represent values on any target orbit. Rather, this mode provides the ability to define a desired launch abort energy condition where, if met, the launch vehicle can glide unpowered if necessary to a determined landing site. Conditions for three cases are listed in Table 11.9.

Table 11.9 Mode 46 Target Orbits

Case	Mode	altitude (km)	velocity (m/s)	i (deg)	γ_f (deg)
39	46	122	7500	51.6	-1
40	46	122	7500	51.6	-2
41	46	100	7000	40	-1

The results for these three cases are listed in Table 11.10. All methods agree closely, both in optimized coast length and final burn time, however the OTIS trajectories have somewhat lager second burn times resulting in reduced final mass. The initial conditions used for these cases are the same as all previous cases and are conditions taken from a typical ascent. This results in a higher initial altitude than would most likely be experienced in an abort scenario, thus increasing the convergence difficulty. Figure 11.13 shows both the AMS and OTIS altitude and velocity profiles as well as the flight path angle time histories for case 40.

Table 11.10 Mode 46 Results

Case	Method	Coast (sec)	2^{nd} Burn (sec)	Final Mass (kg)
39	OTIS	0.9908	272.5345	2978.1001
	AMS	0.0000	267.9072	3018.4401
	AMS closed-loop	0.1315	265.6799	3035.7000
40	OTIS	0.3931	267.7783	3021.1169
	AMS	0.1763	263.2835	3060.2844
	AMS closed-loop	0.0392	260.8845	3080.9500
41	OTIS	0.9037	226.0943	3398.1224
	AMS	0.0007	222.9545	3425.2613
	AMS closed-loop	0.0318	221.4846	3433.9000

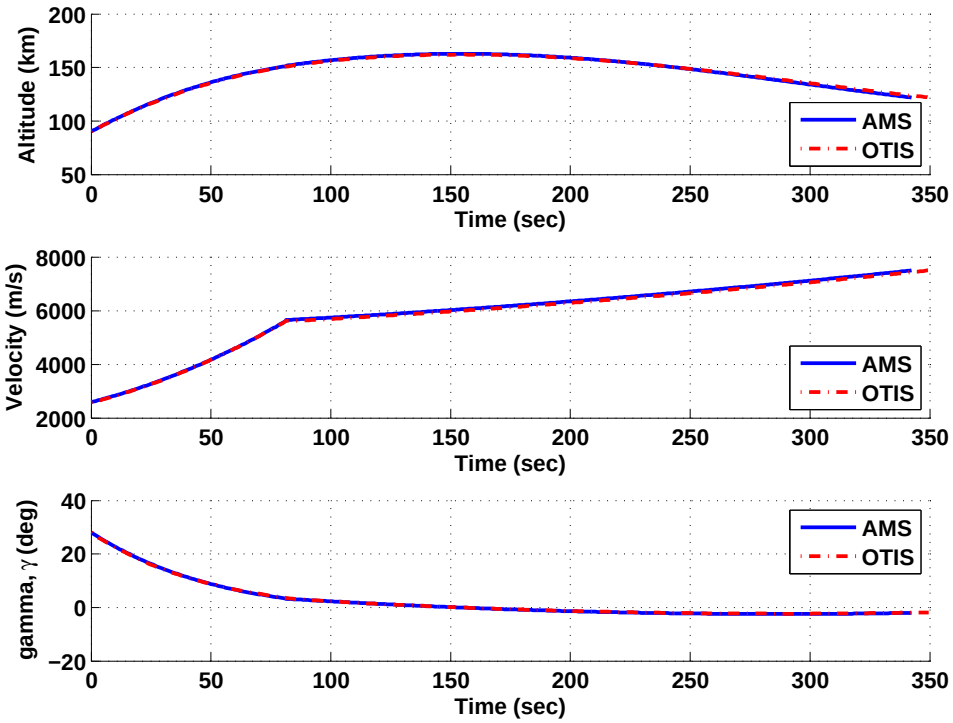

Figure 11.13 AMS and OTIS altitude, velocity, and flight path angle profile comparison for case 40

CHAPTER 12. SUMMARY AND CONCLUSIONS

The Analytical Multiple-Shooting (AMS) method for optimal burn-coast-burn vacuum ascent trajectories is the foundation for the work presented in this thesis. This method maintains the simplicity of traditional single-shooting approaches for exo-atmospheric ascent trajectory optimization while improving robustness by overcoming convergence problems due to increased sensitivity caused in the presence of coast arcs. The optimal launch vehicle vacuum ascent problem formulation is presented in addition to a detailed development of the Analytical Multiple-Shooting approach. Under the burn-coast-burn framework, the ascent trajectory is treated as three segments in which the costate is expressed in closed-form solution and state in analytical solution involving thrust quadratures. Continuity conditions at interior nodes, orbital insertion conditions, and transversality conditions constitute a system of nonlinear algebraic equations with analytic Jacobian.

A strong effort was made to enhance the robustness and reliability of the algorithm. Most notable is the replacement of the modified Newton-Raphson method with the more robust and highly regarded Powell's Dogleg method. This method performed very well and was seen to provide reliable convergence for some situations in which the Newton method could not. The ascending node constraint enforced in modes 41 and 51 was dominate and resulted in increased convergence difficulties where the modified Newton-Raphson method proved insufficient for some scenarios. Powell's method handled this difficult constraint with ease, and for all cases tested was able to converge with no difficulties.

In addition, the f and g series approach to Keplerian motion in the coast arc is replaced by the well established Goodyear's method of orbit determination. The accuracy of the f and g series is limited by a fixed number of terms calculated in the software implementation and

can deteriorate as the coast time increases. This trade-off between general applicability of the algorithm and the programming overhead and complexity inherent in the f and g series approach is alleviated with the use of Goodyear's method. The Goodyear method provided an easily implementable and completely general solution for both the state and its partial derivatives which can be determined to machine accuracy. Concerning the results presented, differences in optimal coast trajectories found from the two methods are indistinguishable which is expected. Expanding the framework to any number of burn / coast combinations, or for interplanetary missions wherein very long duration coast arcs are essential, the methods differences would become much more significant and the generality of Goodyear's method proves very beneficial.

This work also adds the functionality to solve for the unknown Lagrange multipliers directly as part of the nonlinear algebraic equations. This eliminates the need to a priori remove the multipliers from the problem with some numerical or analytical methods. This deemed successful for the majority of terminal modes presented in this paper. This did in some circumstances present convergence difficulties primarily caused by numerical conditioning and scaling issues, however, when feasible, this provided another check on the validity of the current algorithm implementation.

A series of open-loop and closed-loop simulations for different terminal constraint or orbital insertion conditions were explored for a two stage launch vehicle consisting of the "Super X-33" and X-37 vehicles. Similar results between these two simulations demonstrated the effectiveness, robustness, and reliability of the Analytical Multiple-Shooting approach. In addition, the results produced by the AMS method were verified with the industry standard aerospace trajectory optimization software, Optimal Trajectories by Implicit Simulation (OTIS). The extent to which OTIS and AMS matched in terms of the problem objective or vehicle performance determined by deliverable payload mass further verified the AMS algorithm. The variation in optimized coast arc arc solution time resulted in the "flat optimum" characteristic of the ascent problem, approximations made in the AMS approach, flexibility in target insertion orbit found, and in general by the much different methods used by the OTIS and AMS methods as

discussed. In regards to OTIS, the software is very general and allowed for a large amount user configurability. This configurability, however, appears to require an expert knowledge of all its capabilities and its proper use for the desired problem. For the vacuum ascent problem presented in this thesis, the insertion conditions can be enforced by constraining a variety of parameters and it was noticed that changing these parameters can have a significant effect on the optimized trajectory. Additionally, with respect to the coast duration, a slight change in the coast duration guess or even a small change in either the upper or lower bounds containing this guess may cause an unexpected and significant change in the converged result. Also, the upper and lower bounds are not restricting in the sense that a small change in them retains significant margin around the original converged result. Not only does this converged result often change significantly, the difficulty in obtained the solution changes as well. These examples are not to suggest defects in the software, but only to report some notable findings from its use in this work.

The development and resulting necessary equation were presented to expand the burn-coast-burn framework to any number of optimized burn-coast combinations. For single-stage launch missions as well as orbital transfer missions it is desirable to have this capability. Implementing this framework into the AMS algorithm is an evident and beneficial extension of the this work.

BIBLIOGRAPHY

[1] The Space Launch Initiative: Technology to Pioneer the Space Frontier, NASA Marshall Space Flight Center, Pub. 8-1250, FS-2001-06-12-MSFC, June 2001.

[2] Hanson, J. M., "A Plan for Advanced Guidance and Control Technology for 2^{nd} Generation Reusable Launch Vehicles", AIAA Paper 2002-4557, Guidance, Navigation, and Control Conference and Exhibit, Monterey, CA, August 5–8, 2002.

[3] Smith, I. E., "General Formulation of the Iterative Guidance Mode", NASA TM X-53414, March 1966.

[4] McHenry, R. L., Brand, T. J., Long, A. D., Cockrell, B. F., and Thibodeau III, J. R., "Space Shuttle Ascent Guidance, Navigation, and Control", *Journal of the Astronautical Sciences*, Vol. XXVII, No. 1, 1979, pp. 1–38.

[5] Brown, K. R., and Johnson, G. W., "Real-Time Optimal Guidance", *IEEE Transactions on Automatic Control*, Vol. AC-12, No.5, 1967, pp. 501–506.

[6] Brown, K. R., Harrold, E. F., and Johnson, B. W., "Rapid Optimization of Multiple-Burn Rocket Trajectories", NASA CR-1430, September 1969.

[7] Jezewski, D. J., "Optimal Analytic Trajectories", *AIAA Journal*, Vol. 10, No. 5, 1972, pp. 680–685.

[8] Jezewski, D. J., "N-Burn Optimal Analytic Trajectories", *AIAA Journal*, Vol. 11, No. 10, 1973, pp. 1373–1376.

[9] Jezewski, D. J., "An Optimal, Analytic Solution to the Linear Gravity, Constant-Thrust Trajectory Problem", *Journal of Spacecraft and Rockets*, Vol. 8, No. 7, 1971, pp 793–796.

[10] Hardtla, J, W., "Gamma Guidance for Inertial Upper State/IUS/", AIAA Paper 78-1292, Guidance and Control Conference, Palo Alto, CA, August 7–9, 1978.

[11] Gath, P. F., and Calise, A. J., "Optimization of Launch Vehicle Ascent Trajectories with Path Constraints and Coast Arcs", *Journal of Guidance, Control, and Dynamics*, Vol. 24, No. 2, 2001, pp. 296–304.

[12] Calise, A. J., Tandon, S., Young, D. H., and Kim, S., "Further Improvements to a Hybrid Method for Launch Vehicle Ascent Trajectory Optimization", AIAA Paper 2000-4261, Guidance, Navigation, and Control Conference and Exhibit, Denver, CO, August 14–17, 2000.

[13] Dukeman, G. A., and Calise, A. J., "Enhancements to an Atmospheric Ascent Guidance Algorithm", AIAA Paper 2003-5638, Guidance, Navigation, and Control Conference and Exhibit, Austin, TX, August 11–14, 2003.

[14] Lu, P., Zhang, L. and Sun, H., "Ascent Guidance for Responsive Launch: a Fixed-Point Approach", AIAA Paper 2005-6453, Guidance, Navigation, and Control Conference and Exhibit, San Francisco, CA, August 15–18, 2005.

[15] Zhang, L., "A Fixed Point Framwork for Launch Vehicle Ascent Guidance", Ph. D. Dissertation, Department of Aerospace Engineering, Iowa State University, Ames, IA, 2006.

[16] Powell, M. J. D., "A Hybrid Method for Nonlinear Equations", Chapt. 6, *Numerical Methods for Nonlinear Algebraic Equations*, edited by Rabinpwitz, P., Gorden and Breach Science Publisher, Inc., New York, 1970, pp. 87–114.

[17] Goodyear, W. H., "Completely General Closed-Form Solution for Coordinates and Partial Derivatives of the Two-Body Problem", *The Astronomical Journal*, Vol. 70, No. 3, 1965, pp. 189–192.

[18] Goodyear, W. H. "A General Method for the Computation of Cartesian Coordinates and Partial Derivatives of the Two-Body Problem", NASA CR-522, September 1966.

[19] Hargraves, C. R., and Paris, S. W., "Direct Trajectory Optimization Using Nonlinear Programming and Collocation", *Journal of Guidance, Control, and Dynamics*, Vol. 10, No. 4, 1987, pp 338–342.

[20] Optimal Trajectories by Implicit Simulation (OTIS), Volume I – Formulation Manual

[21] Optimal Trajectories by Implicit Simulation (OTIS), Volume II – User's Manual

[22] Gill, P.E., User's Guide for SNOPT Version 7: Software for Large Scale Nonlinear Programming, May 30, 2006.

[23] Bryson, A. E., and Ho, Y. C., *Applied Optimal Control*, Hemisphere, Washington, DC, 1975.

[24] Stoer, J., and Bulirsch, R., *Introduction to Numerical Analysis*, Springer-Verlag, New York, 1993, pp. 125–131.

[25] Bate, R. R., Mueller, D. D., and White, J. E., *Fundamentals of Astrodynamics*, Dover Publications, Inc., New York, NY, 1971, pp. 251-258.

[26] Danby, J. M. A., *Fundamentals of Celestial Mechanics*, 2nd. Edition, Willmann-Bell, Inc., Richmond, VA, 1988.

[27] Lewis, F. L., and Syrmos, V. L., *Optimal Control*, 2nd. Edition, John Wiley & Sons, Inc., New York, NY, 1995.

[28] Pontryagin, L. S., Boltyanskii, V. G., Gramkreledze, Q. V., and Mishchenko, E. F., *The Mathematical Theory of Optimal Processes*, Intersciences, New York, 1962.

[29] Lawden, D. F., *Optimal Trajectories for Space Navigation*, Butterworth, London, UK, 1963.

[30] Lu, P., Griffin, B., Dukeman, G. A., and Chavez, F. R., "Rapid Optimal Multi-Burn Ascent Planning and Guidance", AIAA Paper 2007-6773, Guidance, Navigation, and Control Conference and Exhibit, Hilton Head, SC, August 20–23, 2007.